Fiber Optic Based Thermometry System for Superconducting RF Cavities

Final Report

Sponsored by Department of Energy (DOE), DOE Office of Nuclear Physics (NP), Facilities and Project Management Division

Contract Number: DE-SC0001964

Contractor Name: MicroXact Inc.

Principle Investigator: Dr. Vladimir Kochergin, PI,

Business Address: 295 Industrial Drive Christiansburg, VA 24073

Phone Number: (540) 394-4040

Email: vkochergin@microxact.com

Team members: MicroXact Inc. (lead organization), JLab (partner, internally funded), Virginia Tech (subcontractor), Lake Shore Cryotronics (1st year only, partner, in-kind access to testing facilities).

SBIR/STTR RIGHTS NOTICE

These SBIR/STTR data are furnished with SBIR/STTR rights under Grant No DE-SC0001964. For a period of four (4) years after acceptance of all terms to be delivered under this grant, the Government agrees to use these data for Government purpose only and they shall not be disclosed outside government (including disclosure for procurement purposes) during such period without permission of the grantee, except that, subject to the foregoing use and disclosure prohibitions, such data may be disclosed for use by support contractors. After the aforesaid four year period, the Government has a royalty free license to use all disclosure prohibitions and assumes no liability for unauthorized use of these data by third parties. This Notice shall be affixed to any reproductions of these data in whole or in part.

Table of Contents

1. Executive Summary 3

1.1 Motivation 3
1.2 Accomplishments 3
1.3 Anticipated Public Benefits 4
2. Meeting Project Objectives 5

3. Technical Highlights 6

3.1 Study of thermal expansion of Cu(II)O nano- and micro-particles and composites at cryogenic temperatures: 7

3.1.1 Experimental Methods and Results 8
3.2 Fabrication of negative CTE zirconium tungstate/epoxy composites at cryogenic temperatures 17
3.3 Development of multiplexible fiber optic sensors for cryogenic temperatures: 21
3.4 Testing of fiber optic sensors at Jefferson Laboratory: 28
3.5 Conclusions and outlook 34
4. Products developed under the award and technology transfer activities 35

4.1 Publications: 35
4.2 Web postings: 35
4.3 Networks or collaborations fostered: 36
4.4 Technologies/Techniques: 36
4.5 Inventions/Patent Applications: 36
4.6 Other products: 36

1. Executive Summary

This technical report summarizes the R&D efforts for the DoE-sponsored project "Fiber Optic Based Thermometry System for Superconducting RF Cavities". This research program developed instrumentation for thermal mapping of Superconducting RF Cavities.

1.1 Motivation

Thermometry is recognized as the best technique to identify and characterize losses in SRF cavities. The most widely used and reliable apparatus for temperature mapping at cryogenic temperatures is based on carbon resistors (RTDs). The use of this technology on multi-cell cavities is inconvenient due to the very large number of sensors required to obtain sufficient spatial resolution. In addition, the supply of carbon resistors used in this application has been discontinued. Recent developments make feasible the use of fiber optic sensors for highly distributed temperature measurements. Thousands of Fiber Bragg Grating (FBG) sensors can be inexpensively fabricated on a single optical fiber. However, sensitivity of FBG cryogenic temperature sensors was not sufficient for SRF cavity thermometry. For example, Brillouin scattering-based sensing systems showed +/-6K uncertainty under 12K temperatures (in other words no meaningful temperature readings below 12K is possible with such a technique),[1] Raleigh scattering distributed temperature sensors were claimed[2] to have +/-5K uncertainty at 20K with uncertainly below 20K not reported (it should be noted that due to absence of strain compensation claimed results are of questionable reliability), while Fiber Bragg Grating (FBG) sensors (the most developed multiplexible fiber optic temperature sensing technology) even with special coatings[3] were shown to have some sensitivity only from 12K and above

1.2 Accomplishments

During the course of the project the team of MicroXact, JLab and Virginia Tech developed and demonstrated the first to date multiplexible fiber optic sensor with adequate response below 20K. The demonstrated temperature resolution of developed sensor is by at least a factor of 60 better than that of the best multiplexible fiber optic temperature sensors reported to date. The clear path (by using 60% more expensive and 10 times higher resolution commercial off the shelf interrogation instrumentation) toward at least 10times better temperature resolution is shown, which expects to result in 600 times better temperature resolution than that of state of the art multiplexible fiber optic temperature sensors. The first to date temperature distribution measurements with ~2.5mm spatial resolution was done with fiber optic sensors at 2K to4K temperatures. The repeatability and accuracy of the sensors were verified only at 183K, but at this temperature both parameters significantly exceeded (by at least a factor of 6) state of the art.

Besides the above engineering accomplishments the project resulted in a number of important scientific results. Particularly, it was found and thoroughly verified that giant negative thermal expansion of CuO nanoparticles at cryogenic temperatures[6] does not exist in nature. Further, the negative CTE zirconium tungstate/polymer nanocomposites were obtained at cryogenic temperatures for the first time to the best of our knowledge.

---

[1] S. Mahar et al., "Real-time simultaneous temperature and strain measurements at cryogenic temperatures in an optical fiber," Proc. of SPIE Vol. 7087, 70870I, (2008)

[2] C.D. Boyd, et al., "Monitoring distributed temperatures along superconducting degaussing cables via Rayleigh backscattering in optical fibers," Proc. of the Intelligent Ships Symposium IX (ISSIX) 2011, May 25-26, 2011

[3] R. Rajini-Kumar et al. Cryogenics 48 (2008) 142–147

1.3 Anticipated Public Benefits

The results of this work are expected to find a wide range of applications, since the results are enabling the whole new testing capabilities, not accessible before. For example, the developed sensors can be used for superconducting RF cavity characterization, cryogenic piping monitoring , magnet system control instrumentation for tokamaks and many more. High reliability, multiplexing capabilities, quick response time and low cost per sensing point will provide the means to utilize a spatially denser array of sensors than what is used at present, thus enabling an unmatched to date level of quench detection and localization. Another possible application is LOX and LH2 tanks and lines monitoring (important for NASA). Besides sensing applications, negative CTE composite materials at cryogenic temperatures (achieved on the project) can form the basis for temperature-compensated, inexpensive and easily machinable optical and electronic components for variety of scientific, exploratory and defense applications.

2. Meeting Project Objectives

The following technical milestone were proposed for program:

Milestone 1: Demonstrate experimentally that the proposed nanocomposite coating enhances the resolution/reliability of single FBG sensors at cryogenic temperatures sufficiently to meet the program goals (10mK or better accuracy at 2K-4.3K range).

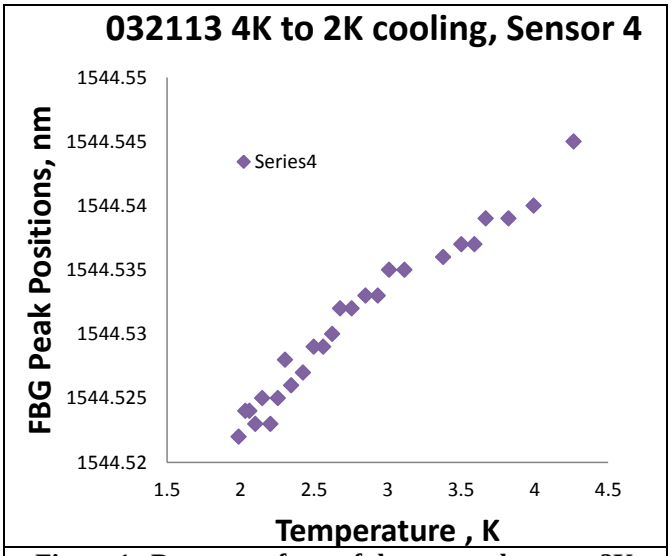

Figure 1. Response of one of the sensors between 2K and 4.3K.

Status: No sufficient testing was done to verify the accuracy of the system at 2K-4.3K range. However, the resolution of better than 100mK was clearly demonstrated at the specified range (by a factor of ~100 better than state of the art for multiplexible fiber optic sensors at these temperatures), the clear path toward the resolution of 10mK was shown at these temperatures, and accuracy better than 100mK at 180K was demonstrated (the lowest temperature at which MicroXact was able to consistently verify the accuracy with the equipment that it had access to).

Milestone 2: Demonstrate experimentally distributed fiber optic temperature sensing on "dummy" can with Nb flat plate.

Status: Truly distributed sensing and thermal mapping was demonstrated at specified experimental conditions.

Milestone 3: Experimentally demonstrate distributed fiber optic temperature measurements with 10mK or better accuracy at conditions similar to those used in SRF cavity testing.

Status: Better than 100mK resolution was demonstrated and the path toward better than 10mK resolution was shown at the specified conditions.

Milestone 4: Demonstrate the performance of distributed fiber optic cryogenic temperature sensor with a “dummy” can and heaters (10mK or better accuracy at 2K-4.3K range).

Status: At 2K to 4.3K the temperature distribution generated by the point heater was demonstrated with two sensors only, as illustrated in Figure 2. This is due to efficient heat removal by supercritical He, which resulted in very localized (just few mm) heating spot (in a proposal stage it was hoped that we will get at least ½ inch).

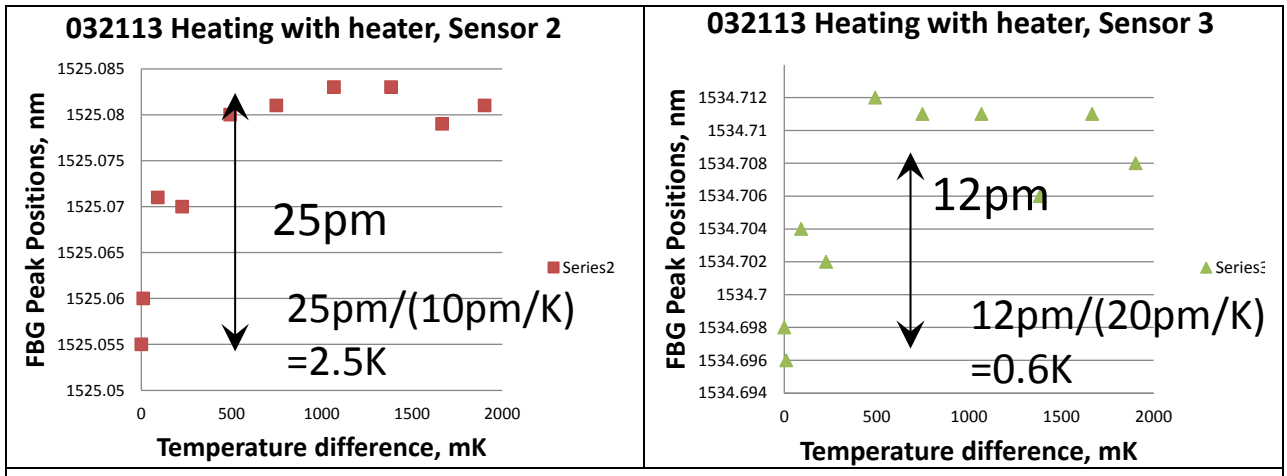

Figure 2. Response of the 2 FBG sensors separated by ~3mm from each other to the localized heating event in Nb can. Starting temperature is ~1.9K.

Milestone 5: Demonstrate fiber optic SRF cavity characterization system that will have the following parameters: 1) sensor density at least as high as with any existing systems, 2) temperature accuracy of 10mK, 3) higher cavity surface coverage than what is available with fixed thermometry systems, and 4) temporal resolution of at least 1Hz.

Status: The system with sensor density as high as with existing systems, temperature resolution of better than 100mK (the clear path toward 10mK accuracy was shown), and temporal resolution of better than 1Hz was achieved on data collection instrumentation. Cavity surface coverage was not achieved since no experiments with SRF cavities were performed. The accomplishments were in-line with reformulated at the end of year 2 project objective.

3. Technical Highlights

The work on the project started with unsuccessful attempts to achieve giant negative CTE of CuO nanoparticles and nanocomposits. ~1.5years of thorough and systematic research confirmed that initially reported effect[6] is probably (pretty much certainly) an experimental bogus. Besides our results, during the work on the project conflicting reports were published on the CTE of this material by other groups as well. For example, 7 nm diameter CuO nanoparticles synthesized with a sol-gel method showed no negative CTE between 1.5 K and 250 K.[4] In a different study, a dense nanoceramic CuO sample displayed only small values of negative CTE, and only within a fairly narrow temperature range of 10K – 40K, with both the CTE values and the temperature range highly dependent on sample granularity.[5] In combination with our results (detail are provided below), this suggests that results reported by Zheng at al. are of skeptical accuracy. Upon verifying it, the team switched to zirconium tungstate/epoxy composites were achieved sizable negative CTE at cryogenic temperatures for the first time. The work then was focused on optimization and testing of fiber optic cryogenic temperature sensors, where the team achieved

[4] Golosovsky, I.V., A.A. Naberezhnov, D.A. Kurdyukov, I. Mirebeau, and G. Andre, Crystallogra. Rep. 56, 164-168 (2011)
[5] Gizhevskii, B.A., E.A. Kozlov, I.B. Krynetskii, and A.Y. Fishman, Low Temp. Phys. 34, 645-647 (2008)

significant success by order of magnitude pushing state of the art sensitivity, resolution and accuracy of multiplexible fiber optic sensing at low temperatures. The detailed description of the results below is following provided above brief summary:

3.1 Study of thermal expansion of Cu(II)O nano- and micro-particles and composites at cryogenic temperatures:

The physical phenomenon on which the proposed concept of cryogenic fiber optic sensing was based was the giant negative CTE of CuO nanoparticles at cryogenic temperatures. A very large negative CTE (-1.1×10^{-4} K^{-1} over 4K-250K range, an order of magnitude larger than in zirconium tungstate) was recently reported by Zheng *et al.* in CuO nanoparticles on the basis of temperature-dependent X-ray diffraction (XRD) studies.[6]

Zheng *et al.* suggested that the observed large negative CTE is of magnetic origin, since the temperature at which the thermal expansion changes sign is roughly the same as the magnetic ordering temperature T_N in bulk CuO. Bulk CuO is an antiferromagnetic compound with two successive phase transitions, undergoing incommensurate ordering around T_{N1} = 230K with a helical period, followed by a first-order commensurate ordering transition around T_{N2} = 213K. A similar thermal anomaly in the magnetic susceptibility of CuO ceramics was reported by Arbuzova et al.[7] They observed an increase in the susceptibility below ~140K as well as the appearance of a paramagnetic-like contribution scaling as $\chi \propto 1/T$ when the grain size in nano-ceramics was reduced below ~70 nm. The observation was tentatively attributed to oxygen vacancies in the measured samples. Magneto-volume effects, where magnetic phase transition are accompanied by changes in the volume of the crystal unit cell, are quite common, and are known to be responsible for large negative CTE values near the Curie temperature in certain materials.[8] The best-known example of this type of effect is seen in the Fe_xNi_{1-x} invar alloys.

In general, the static magnetostriction $\omega_m(T)$ can be written as

$$\omega_m(T) = 3\int \alpha_m(T)dT = \kappa C_{mv}\left\{M(T)^2 + \xi(T)^2\right\}$$

where $\alpha_m(T)$ is the magnetic contribution to the linear thermal expansion coefficient at temperature T, k and C_{mv} are the compressibility and the magneto-volume coupling, and $M(T)$ and $\xi(T)$ are the amplitudes of local magnetic moment and spin fluctuation respectively. Since magnetic susceptibility $\chi(T)$ is proportional to the magnetization per unit field, the behaviour of magnetic susceptibility and thermal expansion can be closely related. The rich magnetic behaviour of CuO therefore makes the existence of large negative CTE in this material quite plausible.

For the studies on this project, we used CuO nanoparticle purchased commercially as well as synthesized chemically or through ball milling of CuO pellets. The particles were subjected to various forms of post processing, including ball milling, electron irradiation, and combustion aided compaction (CAC). A wide range of composite fabrication methods was evaluated as well.

---

[6] Zheng, X.G., H. Kubozono, H. Yamada, K. Kato, Y. Ishiwata, and C.N. Xu, Nat. Nanotechnol. 3, 724-726 (2008)
[7] Arbuzova, T.I., B.A. Gizhevskii, S.V. Naumov, A. Korolev, V.L. Arbuzov, K.V. Shal'nov, and A.P. Druzhkov, J. Magn. Magn. Mater. 258, 342-344 (2003)
[8] Fujita, A., K. Fukamichi, J.T. Wang, and Y. Kawazoe, Phys. Rev. B 68, (2003)

CTE measurements were carried out with both XRD and dilatometry over a temperature range from 20K to 300K. The effect of oxygen vacancies on the CTE of CuO nanoceramics was studied in detail by studying electron irradiated samples of CuO ceramics. None of the samples we investigated displayed a large negative CTE at cryogenic temperatures.

3.1.1 Experimental Methods and Results

3.1.1.1 Cu(II)O Nanoparticle Fabrication

The summary of attempted fabrication methods is provided in Table 1. Three different types of CuO nanoparticles were used: 1) chemically synthesized CuO nanoparticles, 2) commercially available CuO nanoparticles (99.9% purity, American Elements, California USA), and 3) CuO nanoparticles formed by ball milling of commercially available CuO crystalline material (98% purity as purchased, Sigma Aldrich, USA).

Copper Oxide nanoparticles were synthesized with the assistance of microwave radiation by base-catalyzed oxidation of copper acetate in the presence of poly ethylene glycol (PEG) which acts as a surface passivating agent following previously reported synthesis method.[9] Briefly, 0.908 g $Cu(CH_3COO)_2$ (Sigma Aldrich) was dissolved in 25 ml ethanol and combined with a solution of 0.40 g NaOH (Sigma Aldrich) in 25ml ethanol in a 50ml round bottom flask. 0.20 g of PEG (MW 20000) was then added to the solution. The solution was subjected to a microwave process consisting of 20 cycles of 6 seconds of microwaves on and 24 seconds off. The microwave source was a microwave oven operating at 2.45 GHz with a power output of 1 kW, and fit with an external cold water condenser to prevent solvent loss during processing.

Table 1 Summary of attempted fabrication methodologies.

Method of CuO NP Synthesis	CuO NP Post Treatment	Method of forming bulk material
Synthesis	N/A	Composite Fabrication
Synthesis	Functionalization	Composite Fabrication
Synthesis	Ball milling	CAC
Synthesis	N/A	CAC/ Electron irradiation
Synthesis	Ball milling/ Functionalization	Composite Fabrication
Commercial NP	Ball milling	Composite Fabrication, CAC
Commercial crystalline material	Ball milling	Composite Fabrication, CAC
Commercial NP	Cryo ball milling	CAC

The particle size distribution was verified by dynamic light scattering analysis (Nanotrac 250 Particle Size Analyzer, with a detection range of 0.8nm-6.5um). The analysis showed a mostly monodisperse distribution with an average particle size of 7.49nm, as illustrated in Figure 3. TEM imaging (see insert in Figure 3) also confirmed that the CuO particles were mostly in sub-10nm range. UV/Vis absorption spectroscopy of the particle suspension, showed a broad absorption band peaking at 320nm. This corresponds to a band gap of 2.87 eV, which should be compared to a 1.85 eV bandgap in bulk Cu(II)O., which confirms the small size of the particles (below 20nm).

[9] Wang, H., J.Z. Xu, J.J. Zhu, and H.Y. Chen, J. Cryst. Growth 244, 88-94 (2002)

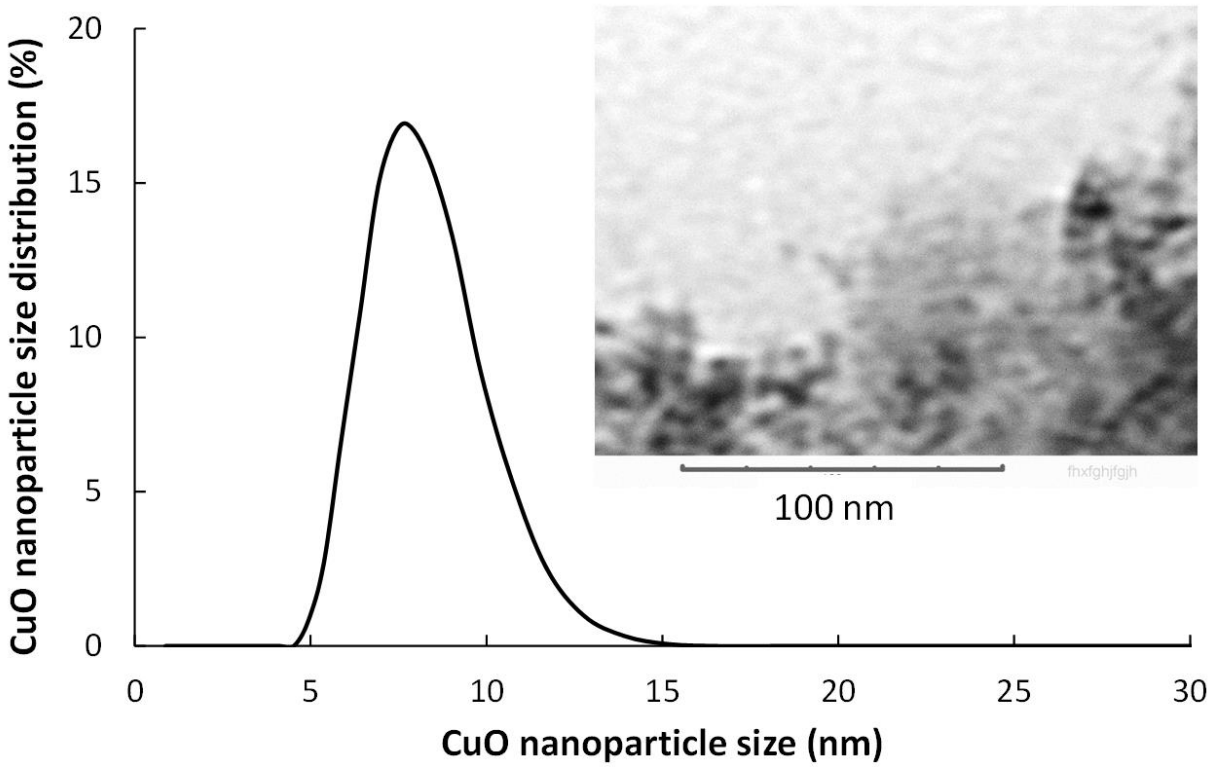

Figure 3. Particle size distribution of CuO nanoparticles dispersed in ethanol solution, verified by dynamic light scattering analysis. The analysis showed a mostly monodisperse distribution with an average particle size of 7.49nm. Insert is showing TEM image of the CuO nanoparticles

Sample purity and crystal structure were determined by X-ray diffraction (Gemini diffractometer from Agilent technologies equipped with a molybdenum X-ray beam source and a cryojet capable of achieving temperatures down to 100K).The XRD pattern of the product obtained is identical to the single phase CuO with a monoclinic structure, as shown in Figure 4. The intensities and positions of the peaks are in good agreement with literature values.[10] A peak broadening is indicative of small particle size. No peak impurities were evident in synthesized CuO.

Commercially available CuO nanoparticles were purchased from American Elements. 40nm average particle size was verified by dynamic light scattering (average particle size was found to be 52.2nm diameter, with a standard deviation of 10nm. XRD characterization of these nanoparticles resulted in less perfect fit of the XRD data to the previously published data on CuO XRD spectrum, which we attribute to impurities and defects in the commercial Cu(II)O powder. Ball milling of these particles reduced their size to 13 nm.

Granular crystalline CuO was purchased from Sigma Aldrich as 99.0% pure pellets, 5-10 mm in diameter. Ball milling of particles for 30hrs was performed to reduce particle size to approximately 1 micrometre as verified by TEM imaging.

[10] FIZ/NIST Inorganic Crystal Structure Database, http://www.nist.gov/srd/nist84.cfm (March 13, 2012)

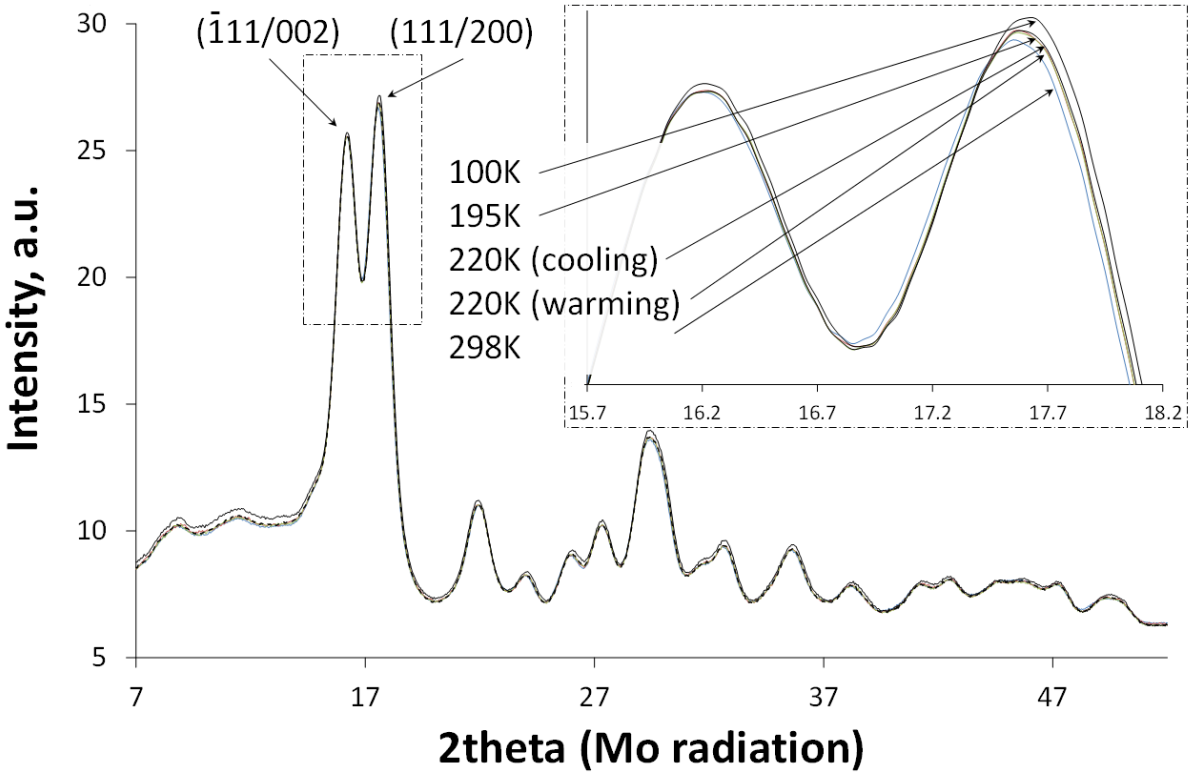

Figure 4. Variable temperature X-ray diffraction data for CuO nanoparticles, ball milled for 10hrs. XRD spectra were collected at 298K, twice at 220K (during cooling and warming cycles), 195K, and 100K. The insert shows the magnified portion of the spectra around (111/002) and (111/200) peaks

3.1.1.2 Cu(II)O nanoparticle post-treatment

Two different methods of CuO nanoparticles post-treatment were used in this study (as listed in Table 1): 1) ball milling, and 2) surface functionalization.

The ball milling of CuO nanoparticles was performed in tungsten carbide milling jars with tungsten carbide grinding balls. The studies were performed at ball mill speed of 350rpm for time intervals of 4hrs, 8hrs, 30hrs, and 160hrs.

Surface functionalization of CuO nanoparticles was evaluated to optimize the adhesion between the CuO nanoparticle surface and the resin to minimize voids and to minimize stress at particle/ resin interface created by different coefficients of thermal expansion of the two materials in CuO/polymer nanocomposites. First, copper oxide nanoparticles were treated with organosilane MPS (3-methacryloxypropyltrimethoxysilane) in order to render particle organophillic. The silane surface treatment was applied by washing the particles in a THF/MPS (0.5 M 3-methacryloxypropyltrimethoxysilane in tetrahydrofuran) solution for one hour followed by centrifugation to remove excess solvent and allowed to dry. High resolution TEM images revealed surface functionalization layer to be ~1nm thick.

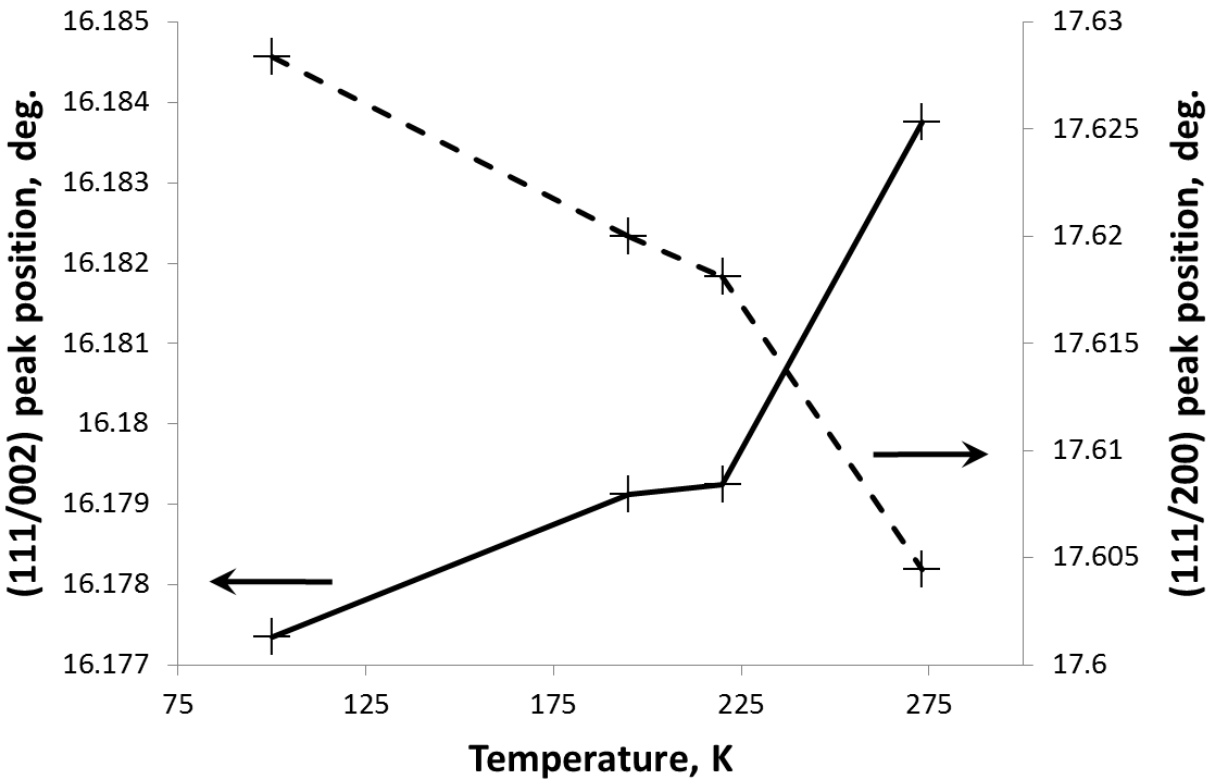

Figure 5. Temperature dependence of CuO XRD (111/002) and (111/200) peak positions recalculated from data shown in Figure 2.

3.1.1.3 Temperature-dependent XRD studies of Cu(II)O nanoparticles

In an effort to reproduce the results by Zheng *et al.*[6] we performed temperature dependent XRD studies of chemically synthesized and/or ball-milled CuO nanopowders. The measurements (shown in Figure 4) were done on CuO nanoparticles with an average diameter of 7.5 nm, and had been ball milled for 10hrs in a planetary ball mill after synthesis. XRD spectra were taken at temperatures above and below the bulk CuO magnetic reordering temperatures of 213K and 230K: at 100K, 210K, 220K (twice, during heating and cooling cycles) and at 300K. The data was processed to extract the temperature-dependent positions of (111/002) and (111/200) peaks, which are typically used for measurements of lattice expansion of Cu(II)O (see [2,3]) and the results of such a data processing are presented in Figure 5. As expected for Cu(II)O, changes in the CTE slope were observed around the magnetic ordering temperatures, , but no change in the sign was detected (*i.e.*, the thermal expansion of Cu(II)O nanoparticles was positive within the temperature range we tested). The observed behaviour was qualitatively similar to that reported by Golosovsky *et al.* [4] and very different from what was reported by Zheng *et al.* [6].

Since the available XRD instrumentation had limited capabilities at low temperatures, we performed much more thorough characterization of CTE of various CuO nanoparticle-based samples using dilatometry, described below.

3.1.1.4 Cu(II)O Nanocomposite Fabrication

As illustrated in Table 1, two principally different types of Cu(II)O nanoparticle-based bulk materials were investigated by dilatometry: 1) Dense CuO nanoceramics fabricated by Combustion Aided Compaction (CAC), and 2) CuO/polymer nanocomposites.

The nanoceramics were fabricated with CAC by Utron Kinetics, Inc. (Manassas, VA, USA). The peak pressure during compaction process was in the 1 GPa to 2 GPa range, and the resulting cylindrical discs were formed into 5x7x9mm coupons. CAC samples were made from both ball milled CuO nanoparticles (at a range of conditions described in previous section) and non-ball milled CuO nanoparticles. Density measurements indicated that samples made of ball-milled particles had 15% porosity while non-ball milled samples had 25% porosity. SEM investigation of such samples (see insert in Figure 7) indicated that the samples were of sufficient quality for dilatometry measurements.

CuO nanoparticle/polymer nanocomposites were fabricated with the following resin systems: Duralco 4460 (Fiber Instrument Sales, USA), Epotek 301-2 (Fiber Instrument Sales, USA) and Stycast 2850FT (Lake Shore Warehouse USA). Low energy ball mill mixing was used to incorporate copper oxide nanoparticles into the resins. Milling jars were filled to 2/3 capacity with glass beads, resin and CuO particles, and the volume fraction of CuO nanoparticles was varied from 0% to 30%. Mixing was accomplished by running the ball mill at 200 rpms for two minutes. The grinding beads were then removed from epoxy, and the resin was poured into 5x7x9mm Teflon molds. These were then degassed at -20psi and room temperature in a vacuum oven for two hours. Finally, the epoxies were cured following the instructions of the manufacturer: Samples made with Epotek resin were annealed at 80°C for 3 hours, those with Duralco resin at 120°C for 4 hours, and those with Stycast resin at 80°C for 4 hours.

3.1.1.5 Dilatometry studies of Cu(II)O nanocomposites

Dilatomery measurements were performed using strain gauges (WK-00-250BF-10C from Vishay Micromeasurement) in a setup based on a Wheatstone bridge shown in Figure 6a. The two strain gauges labeled ‘g1’ and ‘g2’ were affixed to a single piece of titanium, keeping their resistances equal regardless of the temperature. . The ‘reference’ gage (R) was affixed to a material with a known CTE (titanium or titanium silicate). The ‘sample’ gauge (S) was affixed to the CuO composite, which was thermally loosely held in place with tape to minimize external strain. The input (V_{ex}) and output (V_o) voltages on the bridge were measured with lock-in amplifiers, from which the strain in the sample was calculated.

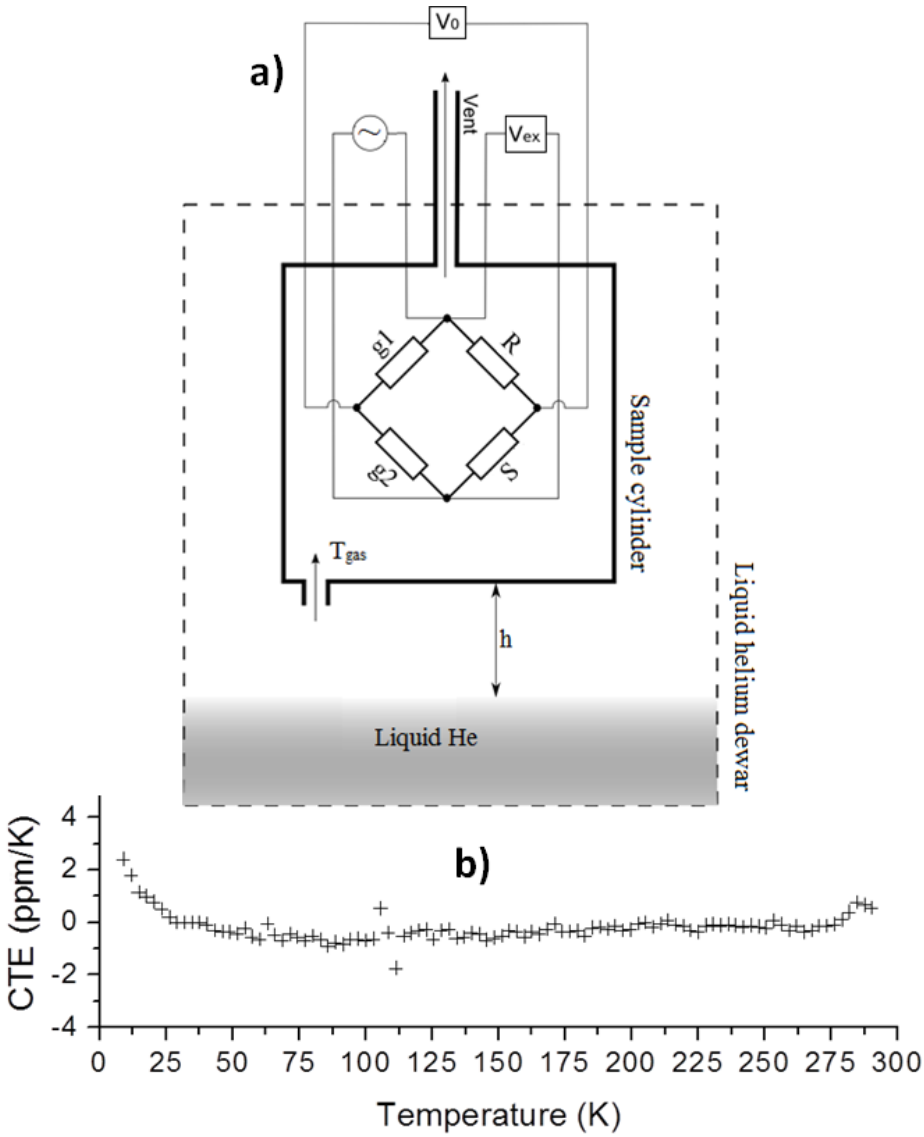

Figure 6. a) Schematic drawing of cryogenic dilatometer; b) Temperature dependence of CTE measurement error of the cryogenic dilatomer, identified as a difference between the measured CTE of oxygen-free copper and tabulated values of CTE of this material provided by NIST.

To measure strain as a function of temperature, the entire assembly (shown in Figure 6a) was slowly lowered into a dewar toward a liquid helium surface. Gas was continually drawn into the sample cylinder to rapidly equilibrate the sample with the ambient temperature, and the strong stratification of the helium gas made it possible to smoothly vary the temperature by adjusting the vertical position of the cylinder. To minimize thermal gradients and enhance the accuracy of the setup, the sample was lowered by means of a stepper motor, maintaining the rate of temperature change at 15 mK/s by an electronic feedback loop.

The sample CTE values were then calculated by taking the derivative of the measured strain curve and subtracting the known CTE of the reference sample. To verify the accuracy of the setup, the CTE of oxygen-free copper was measured and compared to the known NIST

standard[11] (See Figure 6b). These measurements showed that the setup was accurate to within 1ppm/K between 20K and 280K. Accuracy is poor below 20K due to variations in characteristics between gauges, and data for these lowest temperatures should be disregarded.

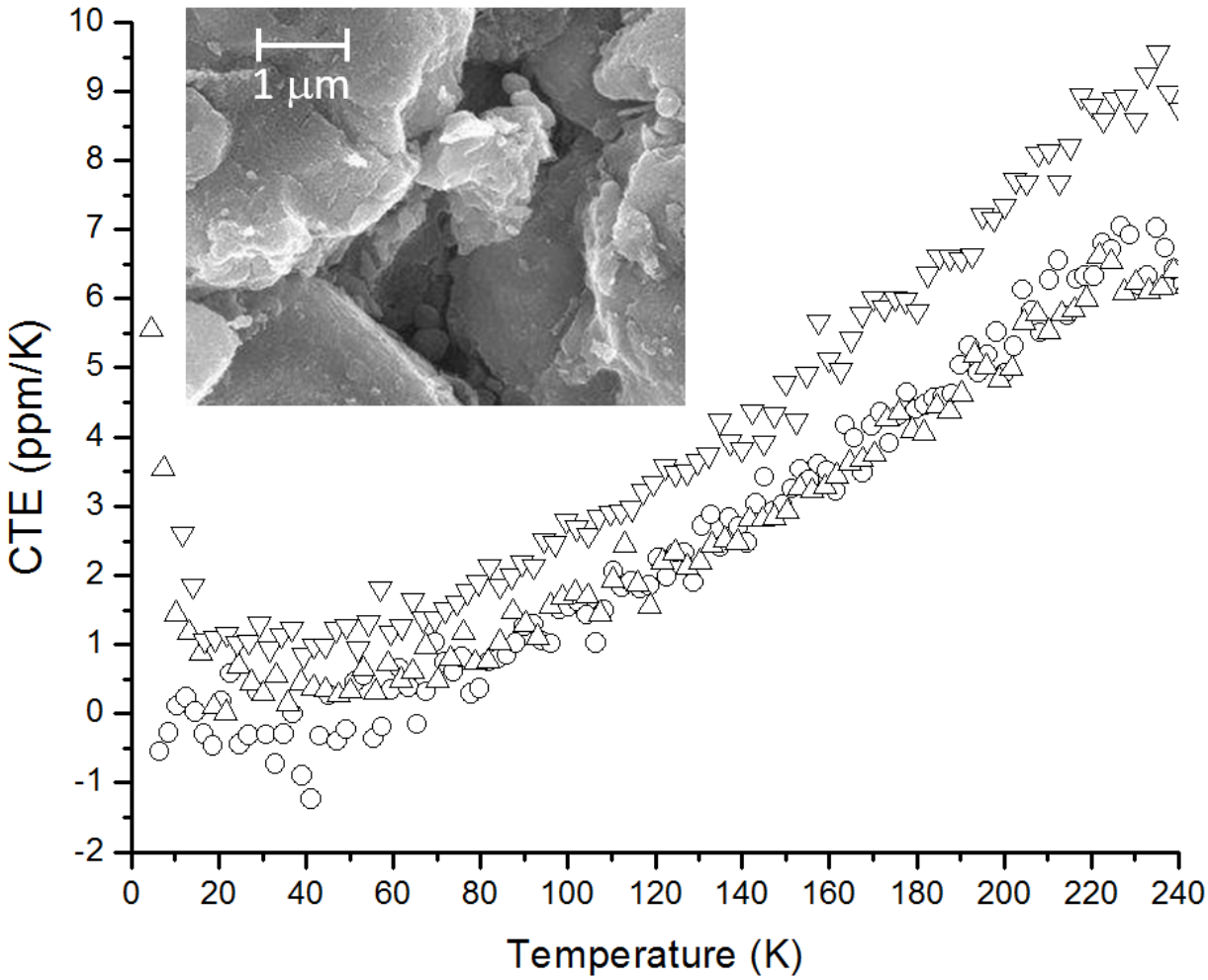

Figure 7. Temperature dependences of CTE in compacted nonirradiated and electron irradiated CuO samples: ▽ - Non-irradiated sample; ○ - Irradiated sample 1; △ - Irradiated sample 2. The insert shows an SEM cross-sectional image of the cleaved compacted CuO sample after cryogenic temperature cycling

Initial testing was done on CAC-processed Cu(II)O nanoceramics. Results of dilatometry measurements of such samples are provided in Figure 7. It is clear that no giant negative CTE occurs in theses samples at cryogenic temperatures. The results are qualitatively similar to those reported by Krynetskii *et al.*[12] and do not display the effect reported by Zheng *et al.*[6]

As was mentioned previously in this report, the thermal expansion of CuO and its magnetic susceptibility may be closely related. Arbuzova *et al.* reported that a thermal anomaly in the magnetic susceptibility of CuO ceramics can be achieved by electron beam irradiation[13] of CAC-

[11] N.J. Simon, E.S.D., and R.P. Reed, Properties of Copper and Copper Alloys at Cryogenic Temperatures,, in NIST Monograph 1771992: National Institute of Science and Technology, Boulder, Colorado. p. 7-23

[12] Krynetskii, I.B., B.A. Gizhevskii, S.V. Naumov, and E.A. Kozlov, Phys. Solid State **50**, 756-758 (2008).

[13] Arbuzova, T.I., S.V. Naumov, V.L. Arbuzov, and A.P. Druzhkov, Phys. Solid State 51, 953-960 (2009)

formed CuO nanoceramics sample, which likely is due to the formation of oxygen vacancies in the CuO material. In order to determine if oxygen vacancies in our ceramics could have similar effects on the thermal expansion, three CuO nanoceramic samples were irradiated with electron irradiation energy 4.5 MeV with the fluence of 1 x 10^{18} e-/cm^2 for 200minutes to achieve the density of defect centers similar to those obtained by Arbuzova et al. E-beam irradiation was performed by E-Beam Services Inc., Lebanon Ohio. While e-beam irradiation indeed had an effect on the CTE of the samples (reducing to near zero or slightly negative values at temperatures below ~70K), we did not reproduce the large negative CTE effect reported by Zheng *et al*. Again, the measurements were qualitatively quite similar to those reported by Krynetskii *et al.* for compacted CuO ceramics.

Results of dilatometry testing of Cu(II)O/polymer nanocomposites is shown in Figure 8. Again, no negative CTE was observed in any of the samples throughout the entire temperature range measured.

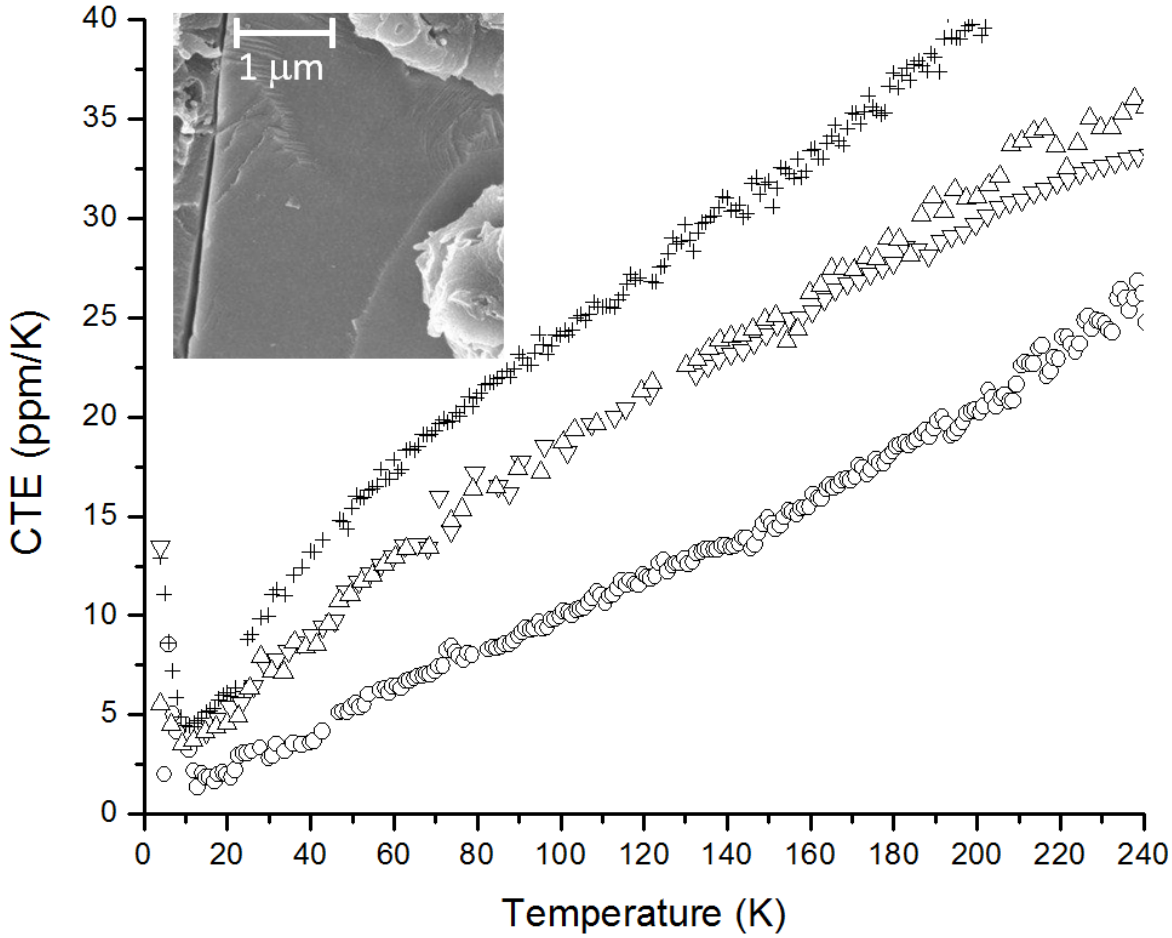

Figure 8. Temperature dependences of CTE in various epoxy/CuO nanocomposites: ○ - 20 vol. % CuO NP's in Stycast epoxy; + - 20 vol. % CuO NP's in Epotek epoxy; ▽, △ - 20 vol % MPS-treated CuO NP's in Epotek epoxy (different samples). The insert shows an SEM cross-sectional image of the cleaved CuO/Epotek nanocomposite sample after cryogenic temperature cycling.

In order to retrieve the CTE of Cu(II)O nanoparticles, we performed curve fitting of the dilatometry data by using the simplest composite effective CTE model[14]

$$\alpha^* = \frac{K_1\alpha_1 V_1 + K_2\alpha_2 V_2}{K_1 V_1 + K_2 V_2}$$

Where α_i are CTEs, V_i are volume fractions, and K_i are bulk moduli of CuO nanoparticles and epoxy matrix respectively. In this model we used the temperature-dependent epoxy parameters provided by respective vendors, and for Cu(II)O nanoparticles we used the temperature dependent values reported for Cu(II)O nanowires.[15,16] Recalculated with this technique CTE of Cu(II)O nanoparticles was found to be in the range of 6ppm/K to 7ppmK at 200K, close to that reported by Krynetskii *et al.*[12] and sizably larger than the 1.6ppm/K that has been reported for single crystal CuO.[17] The close match is an indication of the good quality of our nanocomposites. The results were qualitatively similar for all different nanoparticle fabrication routes, nanoparticle post processing treatments and composite processing steps.

3.1.1.6 Concluding Remarks

We have performed detailed studies of the CTE in CuO nanoparticles and nanocomposites that are in line with the results from CuO nanoparticles by Gizhevskii *et al.* [5] and nanoceramic by Krynetskii *et al.* [12]. While the CTE anomaly at below 70K was indeed observed for the electron irradiated samples, the observed values of negative CTE were no larger than -1 ppm/K, by two orders of magnitude smaller than those reported by Zheng *et al.* It is plausible that the negative CTE we do see is due to conversion of some of the CuO material into Cu_2O which has small negative CTE of -2.4ppm/K between 9 and 240K.[18,19]

The divergence of the magnetic susceptibility of CuO ceramics with large concentration of oxygen vacancies at low temperatures reported by Arbuzova *et al.* [7,13] does suggests that sizable negative CTE of CuO nanoparticles and ceramics is plausible; however, our experimental findings have not confirmed this hypothesis. It does seem to be more logical to explain the observed small negative CTE of the CuO samples by the presence of oxygen vacancies (i.e., defects) in dense nanoceramics. It is also possible that the nature and concentration of such defects is determined by the methods of preparation and processing of the samples. The fact that no group to date has been able to reproduce the results by Zheng *et al.* indicates that there is significant sepsis in the validity of Zheng's results.

---

[14] Schapery, R.A., J. Comp. Materials **2**, 380-404 (1968)
[15] Tan, E.P.S., Y. Zhu, T. Yu, L. Dai, C.H. Sow, V.B.C. Tan, and C.T. Lim, Appl. Phys. Lett. **90**, 163112 -163112-3 (2007)
[16] Ying, X.M. and Y.N. Wang, Physica B 370, 146-150 (2005)
[17] Krynetskii, I.B., A.S. Moskvin, S.V. Naumov, and A.A. Samokhvalov, Jetp Lett. **56**, 566-569 (1992)
[18] Schafer, W. and A. Kirfel, Appl. Phys. A-Mater. Sci. Process. 74, S1010-S1012 (2002).
[19] Sanson, A., F. Rocca, G. Dalba, P. Fornasini, R. Grisenti, M. Dapiaggi, and G. Artioli, Phys. Rev. B 73, (2006)

3.2 Fabrication of negative CTE zirconium tungstate/epoxy composites at cryogenic temperatures

After finding out that the initial concept (CuO-based composites) will not work since it was based on bogus publication (although in the most reputable journal), MicroXact started the search for alternative materials that can form a basis for the fiber coating.

A number of materials with large NTE are known and were recently reviewed by Miller et al.[20] These include cubic ZrV_2O_7,[21] cubic ZrW_2O_8,[22] orthorhombic $Sc_2W_3O_{12}$, and a number of other materials.[23] The α-phase of zirconium tungstate (ZrW_2O_8) has garnered the most interest due to its large, isotropic negative CTE of -9×10^{-6} K^{-1} over a particularly wide temperature range (0.3 K to 400 K). However, all the materials in the class display NTE over a significant temperature ranges. The NTE originates from supramolecular effects, e.g. ferroelectric, magnetostrictive, displacive phase transitions, low frequency phonon modes, etc. In the case of ZrW_2O_8 it is believed to be caused by the crystal structure admiting more degrees of freedom than there are constraints, which allows low-lying rigid unit modes[24] (RUMs) to be excited from the transverse thermal motion of metal-oxygen-metal (M-O-M) bonds. In addition, the tight metal-oxygen bond in ZrW_2O_8 ceramics means that longitudinal M-O vibrations only give rise to a small positive contribution to the CTE, so that the negative contribution from the RUMs dominates the thermal expansion. The most important for us property of α-ZrW_2O_8 is that it exhibits large negative CTE to very low temperatures (0.3K), thus giving us some hope that if fiber optic sensor based on this material will be realized, it will also have sizable sensitivity down to sub-1K temperatures, by more than an order of magnitude lower temperatures that any state-of-the-art multiplexible fiber optic temperature sensors.

High cost and fabrication challenges associated with making bulk α-ZrW_2O_8 have limited the applications of this and other NTE materials. Instead, much of the effort in this area has been directed a polymer composites with α-ZrW_2O_8 used as a filler to tailor the CTE. Such composites cost less to produce, are easier to form and machine, and may also have more favorable mechanical properties than the pure ceramic. Examples include composites based on epoxy,[25,26] polyester,[25] phenolic,[27] polyimide,[28,29] and cyanate ester[30,31] resin systems. In all cases, addition of zirconium tungstate significantly reduces CTE near room temperature, but NTE has previously not been reported. In the following section we are describing how such a property of zirconium tungstate can be realized.

The composite was fabricated with a two part epoxy, using EPON 862 resin and EPIKURE Curing agent W (Momentive Specialty Chemicals Inc). ZrW_2O_8 was purchased as an 8 μm

---

[20] W. Miller et al., J. Mater. Sci. 44, 5441 (2009)
[21] V. Korthuis et al., Chem. Mater. 7, 412 (1995)
[22] T. A. Mary et al., Science 272, 90 (1996)
[23] J. S. O. Evans, T. A. Mary, and A. W. Sleight, J. Solid State Chem. 133, 580 (1997)
[24] A. K. A. Pryde et al., Phase Transitions 61, 141 (1997)
[25] J. D. Shi et al., Proc. Mat. Res. Soc. 445, 229 (1996)
[26] W. Miller et al., Phys. Status Solidi B 245, 552 (2008)
[27] J. Tani et al., J. Appl. Polym. Sci. 106, 3343 (2007)
[28] L. M. Sullivan, and C. M. Lukehart, Chem. Mater. **17**, 2136 (2005)
[29] C. Lind *et al.*, Phys. Status Solidi B **248**, 123 (2011).
[30] P. Badrinarayanan, and M. R. Kessler, Compos. Sci. Technol. 71, 1385 (2011)
[31] W. C. Weyer *et al.*, in *Proceedings of the 46th AIAA/ASME/ASCE/AHS/ASC Structures, Structural Dynamics & Materials Conference* (AIAA, Austin, TX, 2005), p. 3577

average particle size powder from Alfa Aesar. To ensure that the tungstate was in the α-phase, we found it necessary to anneal the powder for six hours at 800 °C in a nitrogen atmosphere followed by rapid quenching to room temperature. The phase was confirmed by X-ray powder diffraction on a Gemini diffractometer from Agilent Technologies equipped with a molybdenum X-ray source. After annealing, particles were treated with 0.1wt% of the surfactant Triton-X-100 to prevent auto-hydration–a kinetically slow but thermodynamically inevitable reaction which has been shown to occur after 1-2 days of exposure to ambient conditions[32]–and to promote dispersion of the particles within the epoxy resin system.

The composite was formed by mixing the ZrW_2O_8 powder with the resin at 200 rpm for 15 min in a planetary ball miller. This enabled us to fabricate uniform composites with relatively high (>20 vol. %) loadings of tungstate. SEM images of ZrW_2O_8/epoxy composites fabricated with this technique is shown in Figure 9, where the good mixing uniformity is apparent.

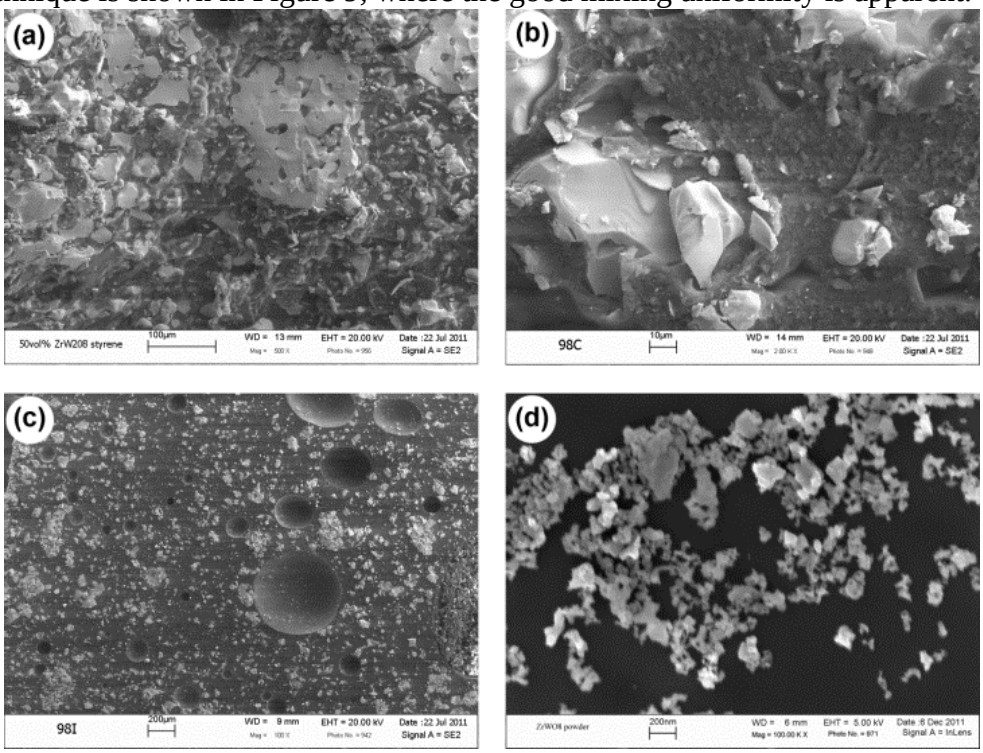

Figure 9. SEM images of ZrW_2O_8/epoxy composite samples showing microstructure of (a) 50 vol.% loading, scale bar 100 µm; (b) 30 vol.%, scale bar 10 µm (c) 20 vol.%, scale bar 200um; and (d) ZrW_2O_8 powder (no epoxy), scale bar 200 nm

To maximize the tungstate filling and thereby the NTE, we took advantage of the tendency of the ceramic particles to settle in the resin before curing by leaving the uncured epoxy/tungstate mixture at room temperature for 24 hours prior to curing, followed by a slow cure at 60 °C for an additional 24 hours. The top portion of the sample was sanded down to remove the sections of the epoxy with low tungstate filling. During this process, the density of the sample was measured periodically, and sanding was continued until the density of the sample had stabilized, which typically occurred for densities in the range of 3.4-3.6 g/cm^3, which corresponds to a tungstate filling of 59-64 vol.%.

[32] L. C. Kozy et al., J. Mater. Chem. 19, 2760 (2009)

We model the coefficient of thermal expansion in the composite using the model due to Schapery.[33] Based on variational principles, this model predicts that for a two-component composite

$$\hat{\alpha} = \frac{K_2\alpha_2(\hat{K} - K_1) - K_1\alpha_1(\hat{K} - K_2)}{\hat{K}(K_2 - K_1)}$$

where α and K are linear coefficients of thermal expansion and bulk moduli, respectively. The subscripts indicate the properties of the constituent phases, while the quantities with carets represent the properties of the composite. The composite bulk modulus $\hat{K}$ can be estimated using the variational model of Hashin and Shtrikman.[34] If $K_1 > K_2$, then the upper bound on $\hat{K}$ is given by

$$\hat{K}^{(+)} = K_1 + \frac{v_2}{\frac{1}{K_2 - K_1} + \frac{v_1}{M_1}}$$

where M_i (sometimes also written C_{11}) and v_i are longitudinal moduli and the volume fractions of each of the phases in the composite. The lower bound $\hat{K}^{(-)}$ is found by interchanging the subscripts 1 and 2 everywhere in above equation. For the case at hand, the CTE for zirconium tungstate was extracted from Ernst et al.[35] and the elastic moduli for the tungstate were taken from the work by Drymiotis et al.[36] For the epoxy, we used the CTE given by our measurements, while the bulk modulus and Poisson's ratio at room temperature were taken to be 2.9 GPa[37] and 0.36, respectively. We do not know these values at lower temperatures, but we can arrive at a valid approximation by noting that amorphous polymers tend to have very similar mechanical properties at low temperatures,[38] so that we can for instance expect the low temperature limit for the bulk modulus of the epoxy to be approximately 8 GPa.[39,40] The epoxy undergoes a secondary glass transition between approximately 100 and 200 K, where the mechanical moduli transition between their high and low temperature values. We do not know the glass transition temperature for our epoxy, but as the model is relatively insensitive to it, we elect to approximate the temperature dependence of the epoxy bulk modulus with the known values of an epoxy with similar stiffness (epoxy 2 in Fig 5. in Hartwig[38]). Poisson's ratio for the epoxy was taken to be 0.36 at all temperatures, consistent with literature reports.[41]

---

[33] R. A. Schapery, J. Compos. Mater. 2, 380 (1968)
[34] Z. Hashin, and S. Shtrikman, J. Mech. Phys. Sol. 11, 127 (1963)
[35] G. Ernst et al., Nature 396, 147 (1998)
[36] F. R. Drymiotis et al., Phys. Rev. Lett. 93, 025502 (2004)
[37] J. L. Tack, in Chem. Eng. (Texas A&M University, 2006)
[38] G. Hartwig, Polymer Properties at Room and Cryogenic Temeperatures (Plenum Press, New york, 1994), he International Cryogenics Monograph Series
[39] H. Cease, in Fermilab Technical Memos TM-2366-A (Fermilab, 2006).
[40] G. Hartwig, in Nonmetallic Materials and Composites at Low Temperatures, edited by A. F. Clark, R. P. Reed, and G. Hartwig (Plenum Press, New York, 1979), pp. 33
[41] I. Perepechko, Low-Temperature Properties of Polymers (Pergamon Press, 1980)

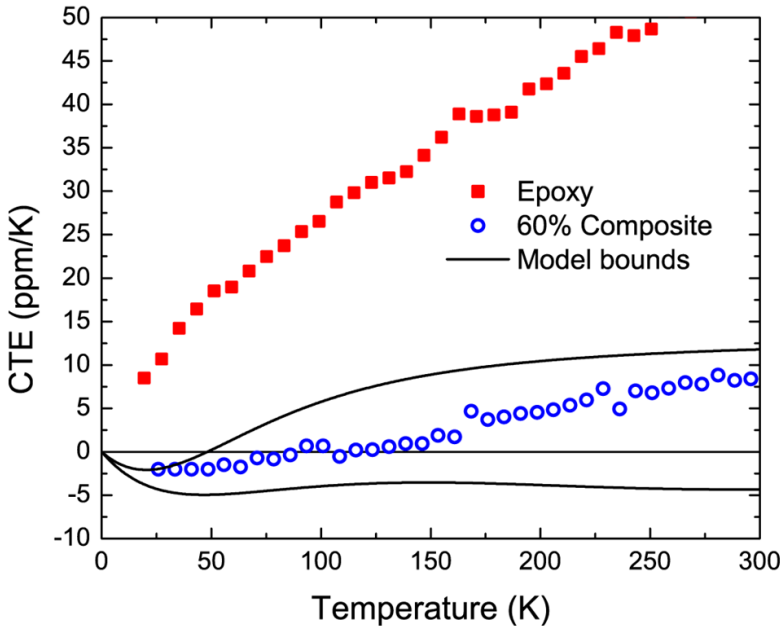

Figure 10. Linear coefficient of thermal expansion in pure EPON 862/W epoxy (red filled squares) and a 60% composite with zirconium tungstate (empty blue circles), showing negative thermal expansion below about 100 K. Upper and lower theoretical bounds for the epoxy are indicated by solid lines

With these values, the model predicts that the composite may not display NTE at any temperature, unless the tungstate filling exceeds 30 vol.%, and significant NTE may not occur until the tungstate exceeds 50% of the composite. For this reason, CTE measurements were performed on the high tungstate filling samples described above.

Thermal expansion was measured between 25 K and 300 K using a dilatometry technique was measured with the same setup and described previously in this report. The strain measured during the cooling of a 60 vol.% tungstate sample is converted in a CTE and plotted in Figure 10 compared to a pure epoxy sample. The upper and lower limits of $\hat{\alpha}$ as predicted by equations provided above are also plotted as solid lines.

The CTE of the composite falls within the bounds given by the model at all examined temperatures, becoming negative below about 100 K. At higher temperatures, the CTE is positive, but is greatly reduced compared to the CTE of the pure epoxy, reaching values typical of glass and ceramics.

Due to equipment limitations, we did not perform measurements below 25 K, but as our model predicts, there is every reason to believe the NTE behaviour of the composites persist down to very low temperatures. This is because the low energy of the RUM modes leads to an Einstein temperature that is significantly lower in ZrW_2O_8 (approx. 25 K)[42] than in the epoxy (70-80 K),[43] which should compensate for the non-Debye behavior of the CTE in amorphous polymers below 30 K.[38] Given that the elastic moduli of both phases are close to constant at low temperatures, this means that the tungstate should continue to dominate the CTE.

With such a results MicroXact started working on fiber optic sensors.

[42] F. R. Drymiotis et al., Phys. Rev. Lett. 93, 025502 (2004)
[43] R. Simha, J. M. Roe, and V. S. Nanda, J. Appl. Phys. 43, 4312 (1972)

3.3 Development of multiplexible fiber optic sensors for cryogenic temperatures:

Initially we attempted embedding of the fiber with FBG into the composite, however, reliable sensor fabrication was never achieved with such a method. Instead of that the composite coupons were fabricated and the fiber with FBG was mounted onto the coupons with epoxy. This fabrication method finally provided reliable fabrication technique. Most probably fiber was disturbing nanoparticle settling while attempting to embed it. Several epoxies were evaluated and Araldyte and 5-minutes epoxy were found to provide the most reliable results.

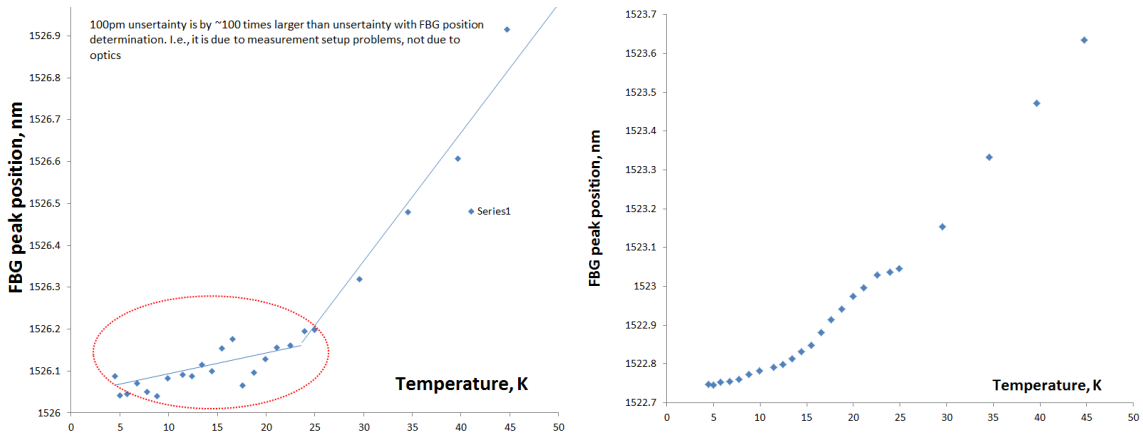

a) b)

Figure 11: FBG peak position as a function of the temperature recorded by a reference RTD sensor a) before optimization of the calibration setup, b) after optimization of calibration setup.

Figure 11 shows sample sensor response at cryogenic temperatures. It should be noted as the resolution/repeatability of the sensors improved, previously used testing and data processing became insufficient and the improvements were made, as it is apparent from Figure 11b. Still it should be noted that the calibration and testing setup that was built during this project (based on sensor "dipping" into He tank, as described previously) is not accurate enough especially at low temperatures: we don't believe that the change of slope at ~23K is "real".

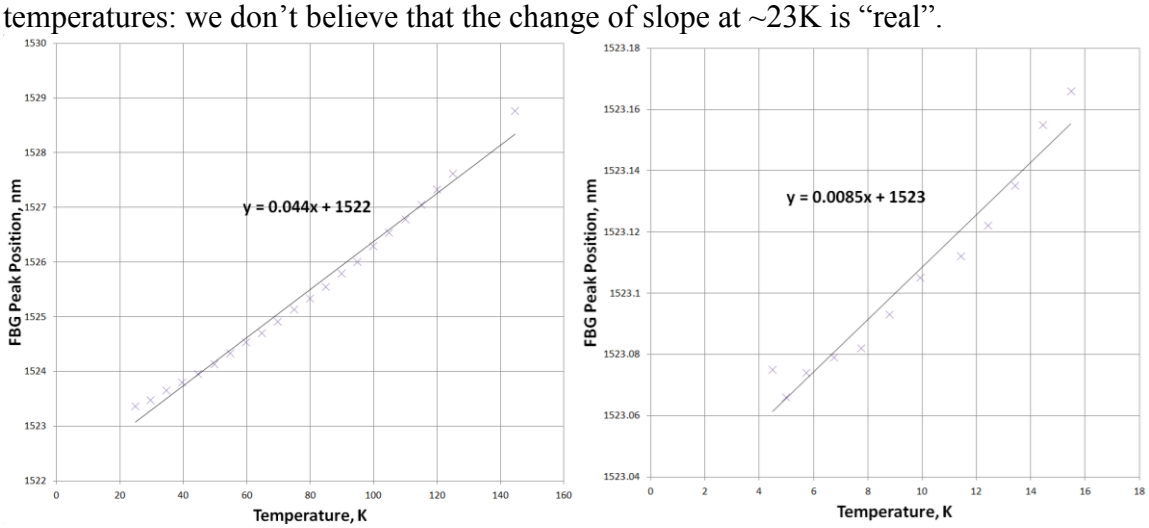

a) b)

Figure 12: Different temperature sensitivities of developed FBG sensor at different temperatures retrieved by

linear fitting of the corresponding sections of the data: a) 44pm/K sensitivity at 20K to 140K range, b) 8.5pm/K in the 4.2K-15K range.

In addition the scatter significantly increased below ~6K probably due to turbulence and temperature gradients related to He boiling off during dipping of the bottom surface of the sensor holder. While it is known to MicroXact that the testing setup based on dipping of the sensor into liquid He first and then setting the temperature by heating a sensor is by far more accurate (to fraction of K) then the setup used in this project, the He consumption (~3/4 of the dewar per single temperature run) made this method unsuitable since the funding of the project was not even close to be sufficient to cover the cost of LHe required for multiple calibration runs. In the future, closed cycle refrigerator-based testing and calibration system is clearly the way to go.
Still, the collected data permits identifying sensitivities of the sensors at different temperature ranges, as illustrated in Figure 12. To give a perspective on the significance of the accomplishment, it is worthwhile to cite some recent references by other groups: R. Rajini-Kumar et al.[44] demonstrated below 1pm/K (below the resolution of used equipment) sensitivity below ~12K for the most sensitive metal-coated FBG sensors (compared to 8.5pm/K demonstrated by us at temperatures below 10K), Mahar et al.,[45] claimed +/-6K uncertainty of measurements below 12K for Brillouin scattering –based sensors while Boyd et al.[46] claimed uncertainty of +/-5K in the range of 20K to 70K with no data provided for temperatures below 20K for Raleigh scattering-based sensors. With 1pm spectral resolution of interrogation instrument (~$15k interrogation instrument from Micron Optics) 8.5pm/K sensitivity of our sensors would result in ~0.1K resolution of the sensor at 4.2K-10K range, while 0.1pm spectral resolution (~$25k-$30k instrument from Micron Optics or ~$100k instrument from Luna Innovations) this would correspond to ~10mK resolution of our sensor, <u>by at least 100s of times better than what was achieved by other groups!</u>

In order to calculate the resolution of the sensor vs. temperature and also in order to identify the best calibration procedure for the sensors we did few curve fits of the data starting from 30K (as was mentioned previously the data ~23K-25K showed some suspicious changes in the slope which we believe were not real and due to problems with calibration setup rather than being an inherent feature of the sensors). We found that the 3rd order polynomial fit (shown in Figure 13) being an optimum since 4th and higher order polynomial fits provided only marginal improvements in fit quality. In terms of calibration, it means that at least 4 point calibration is required for the sensor, with ~6 point calibration providing the adequate accuracy.

[44] R. Rajini-Kumar et al. Cryogenics 48 (2008) 142–147
[45] S. Mahar et al., "Real-time simultaneous temperature and strain measurements at cryogenic temperatures in an optical fiber," Proc. of SPIE Vol. 7087, 70870I, (2008)
[46] C.D. Boyd, et al., "Monitoring distributed temperatures along superconducting degaussing cables via Rayleigh backscattering in optical fibers," Proc. of the Intelligent Ships Symposium IX (ISSIX) 2011, May 25-26, 2011

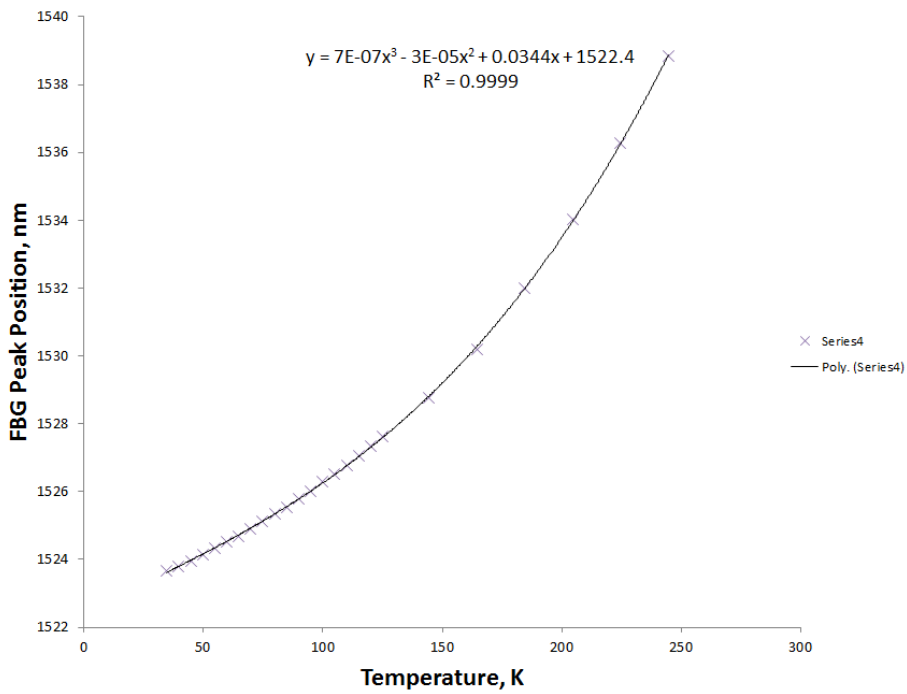

Figure 13: FBG peak position vs. temperature and 3rd order polynomial fit of the experimental data.

The fit was used to calculate expected temperature resolution of the sensor, as shown in Figure 14. One can see that with adequately priced interrogation instrument from Micron Optics the resolution at low temperatures is expected to be in the mK range, sufficient to meet requirements of quench detection in superconducting RF cavities.

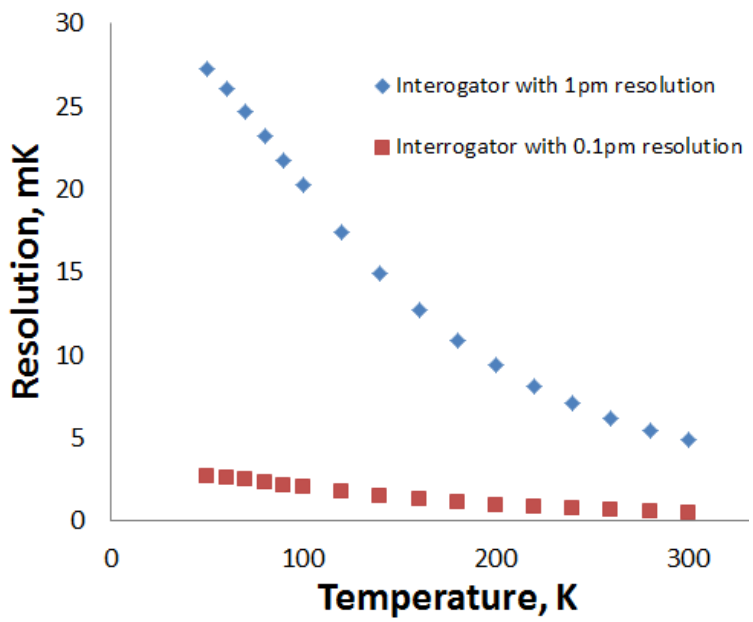

Figure 14: Calculated resolution of developed on this program FBG sensor vs. temperature using 3rd order polynomial fitting function as in Figure 13 and different spectral resolutions of interrogation instrument.

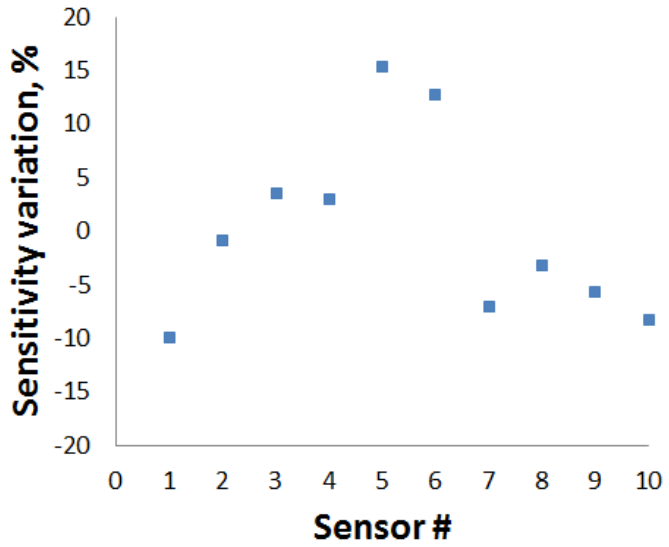

Figure 15: Sensitivity variations of different sensors.

A number of sensors were tested to get a statistics on sensor sensitivity variations (pm/K) between sensors. The results are provided in Figure 15. One can see that majority of sensors are falling within +/-10% sensitivity difference, adequate for commercial applications and drastic improvement over binary statistics that we saw at the beginning of efforts (where sensors were either adequately sensitive or not sensitive at all at cryo temperatures).

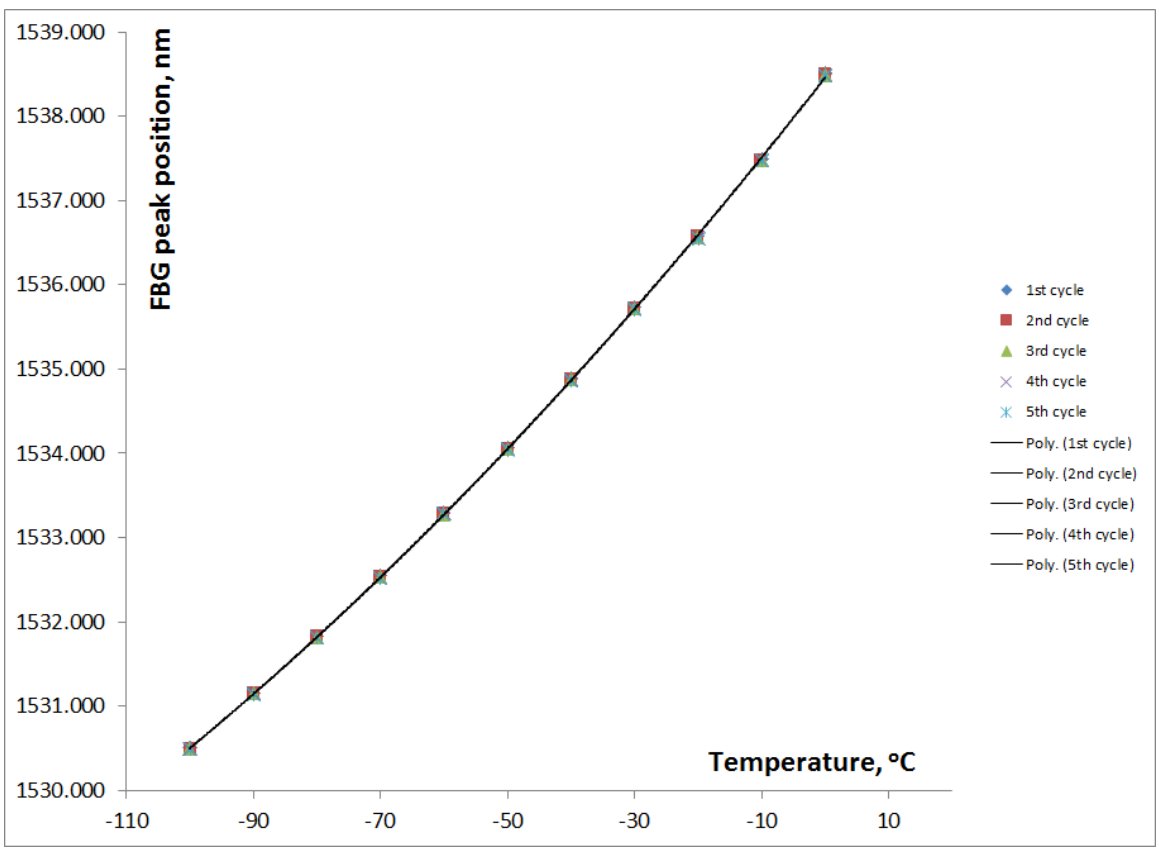

Figure 16: Temperature cycling of developed sensors at reasonably accurate thermal chuck from Instec Inc.

It should be noted that temperature resolution without adequate repeatability and stability of the sensor means very little. The setup that was used for testing and calibration of sensors down to 4.2K was not sufficiently accurate and thus not adequate for testing of these parameters for the following reasons: 1) some unexpected features appeared ~23K, 2) the scatter at the FBG peak wavelength data at low temperatures was by far larger than expected 1pm from interrogation instrument that was used. For this reason different setup was used to study repeatability and stability of the sensors. We used thermal chuck HCC206R with mK1000 controller from Instec Inc.. The temperature accuracy and stability of such a chuck are between 10mK and 100mK at ~-90°C (compared to probably 100mK to 1K for cryogenic setup that was used previously). The chuck does not operates properly at cryogenic temperatures, however, the data can be extrapolated to colder temperatures by taking into account previously reported temperature dependence of sensitivity of developed sensors.

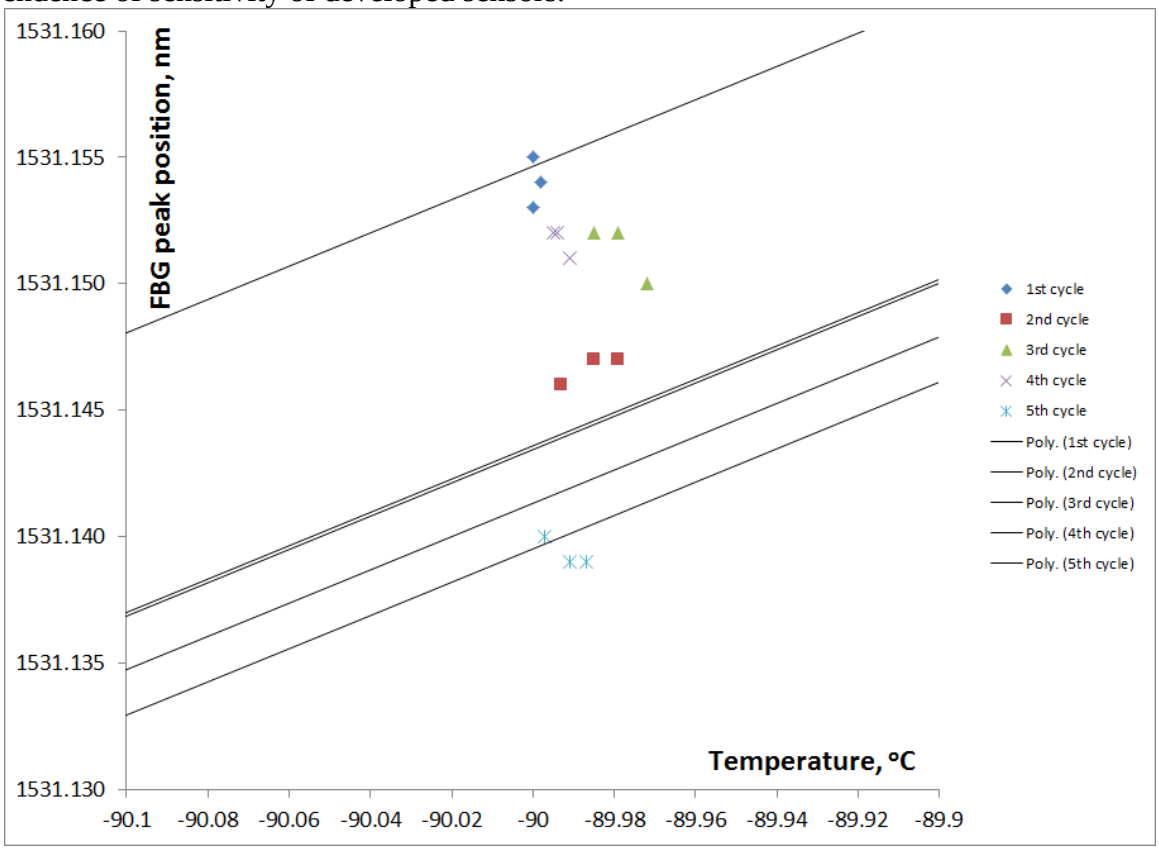

Figure 17: Close-up of temperature cycling of developed sensors at reasonably accurate thermal chuck from Instec Inc around -90°C.

The collected data for 5 cycles is shown in Figure 16 and Figure 17. During testing the chuck was set at each individual temperature (with 15min wait for temperature stabilization), three measurements were taken each 30s. One can see that variations between subsequently taken measurements are within +/- 1pm, consistent with specifications of the spectral resolution of interrogation instrument used. At these temperatures these variations correspond to +/-12mK accuracy. The variations between cycles were quite a bit larger, within+/-8pm and exhibited a random character rather than a trend. These variations correspond to +/-96mK, within the range of expected temperature variations of the thermal chuck. Based on this information it can be stated that stability and repeatability of developed temperature sensors are better than the

accuracy of the testing setup. We do expect the repeatability to be around ~1pm as well (corresponding to ~10mK with used inexpensive interrogator), although we are missing accurate enough calibration instrumentation to experimentally prove it. Based on such a testing it can be with confidence stated that the scatter observed with initial setup below 6K is due to testing setup, not due to sensors.

With such a gratifying results the work on single sensors concluded and development of temperature mapping applique has started. The following characteristics of the applique were required: 1) ease of installation at JLab, 2) security of the fiber, 3) free access of LHe through applique, 4) reasonable mechanical stability. After few trials and errors we come up with the applique shown in Figure 18, where sensors are epoxies to PTFE mesh.

Figure 18: Fiber optic cryogenic FBF sensor applique ready for testing.

Figure 19: Fiber optic thermal mapping testing system with thermal chuck controller, tunable laser operated by the netbook and power supply to provide localized heating. Thermal chuck, FBF sensor applique and point heat source are in nitrogen-purged environmental enclosure to eliminate icing.

To demonstrate thermal mapping in house we used the setup shown in Figure 19: the applique was affixed with Capton tape to the Instec thermal chuck and the point heater (the stainless rod with Nichrome wire wrapped around) was used to apply localized heat at different locations as illustrated in Figure 20.

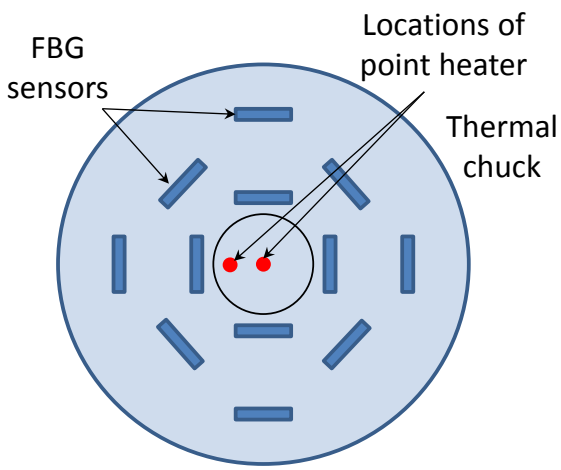

Figure 20: Schematics of thermal mapping experiment on a thermal chuck. Positions of point heating are indicated.

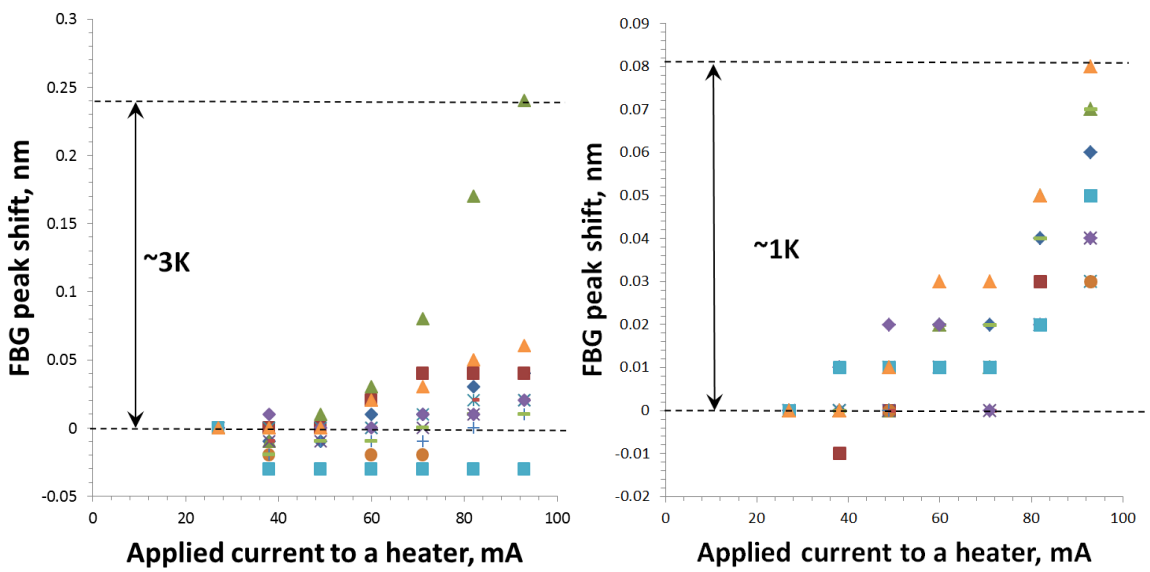

a) b)

Figure 21: FBG peak shifts for the sensors in an array in experiment illustrated in Figure 20 for the cases of a) pint heat source in the left position, and b) point heat source in the center position.

The results of such experiments are shown in Figure 21, where it is clearly seen that temperature distribution in the chuck shifts depending on where the heat is spatially applied. With such a results the work was shifted toward actual demonstration of the sensor performance at Jefferson Laboratory.

3.4 Testing of fiber optic sensors at Jefferson Laboratory:

During the project the total of three testing sessions were performed at JLab. The schematic drawing of the setup used to test the sensors in all three sessions is provided in Figure 22. The resistive heater (constantan wire epoxied around a 1 mm diameter Cu post) makes a spring-loaded contact to the back (vacuum) side of a 3 mm thick Nb plate, generating a controlled temperature increase in the center of the plate with the "size" of the heating spot becomes dependent on heater power, particularly when T_{max} goes above lambda point (2.17K). The reference RTD was also mounted exactly at the center of the front (liquid helium) side of the plate.

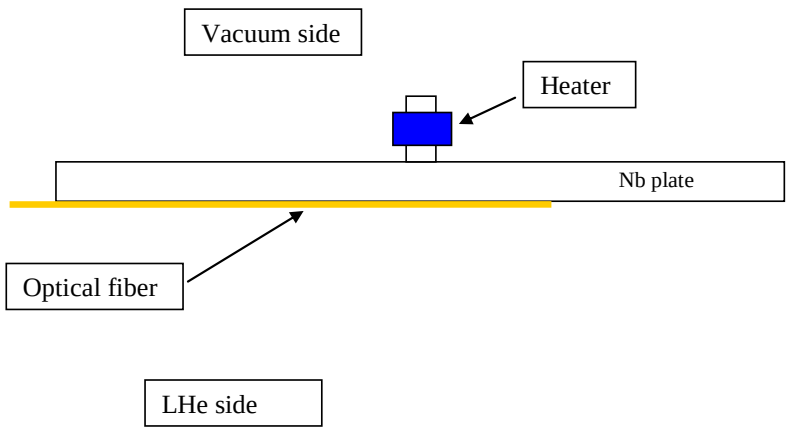

Figure 22. Schematics of the testing setup at JLab. Nb plate instrumented with the heater on the vacuum side was instrumented with FBG sensors and reference carbon glass RTD at the liquid He side.

Reflection spectra were retrieved upon completion of the installation at 300K, upon filling the cryostat with LHe and stabilizing at 1.98K according to RTD readings). During changing the temperature between 1.98 and 4.3K at each temperature step we were waiting for temperature to stabilize according to RTD readings and then performed measurements with fiber optic instrumentation. It should be noted that unlike the RTD readings which has an integration time of ~1s (corresponding to pretty large averaging), the sampling time of FBG sensors was ~10ms total (corresponding to ~1ms per FBG) and no averaging of the data was performed (i.e., we present here "raw" data).

During 1st and 2nd testing it was identified that the area on the bottom surface of the Nb flange heated by the heater is smaller than originally anticipated, with the radius of ~1cm where any detectable temperature change will be expected (initially we expected it to be ~1 inch radius) due to very efficient heat removal by superfluid He. So the sensor mesh as in Figure 18 was not adequate for the task since no temperature change occurred due to the heater at any sensor position.

For this reason the experimental arrangement was modified to what is illustrated in Figure 23. In such an arrangement the set of 4 FBG sensors with different wavelengths was packaged into a single package, with intro-sensor separation of ~3mm, and the lateral separation of the closest to the heating spot sensor of about 3mm as well. The sensor package was placed side-by-side with reference carbon RTD that was calibrated and used while doing testing between 2K and 4K. Both the package with fiber optic sensors and RTD were coated with Apiezon N grease and a spring-loaded contact was used to ensure better thermal contact between the sensors and Nb flange. The PTFE mesh was employed for permanently holding fiber and fiber connector. The arrangement was convenient to mount (it took within 5 minutes to install it).

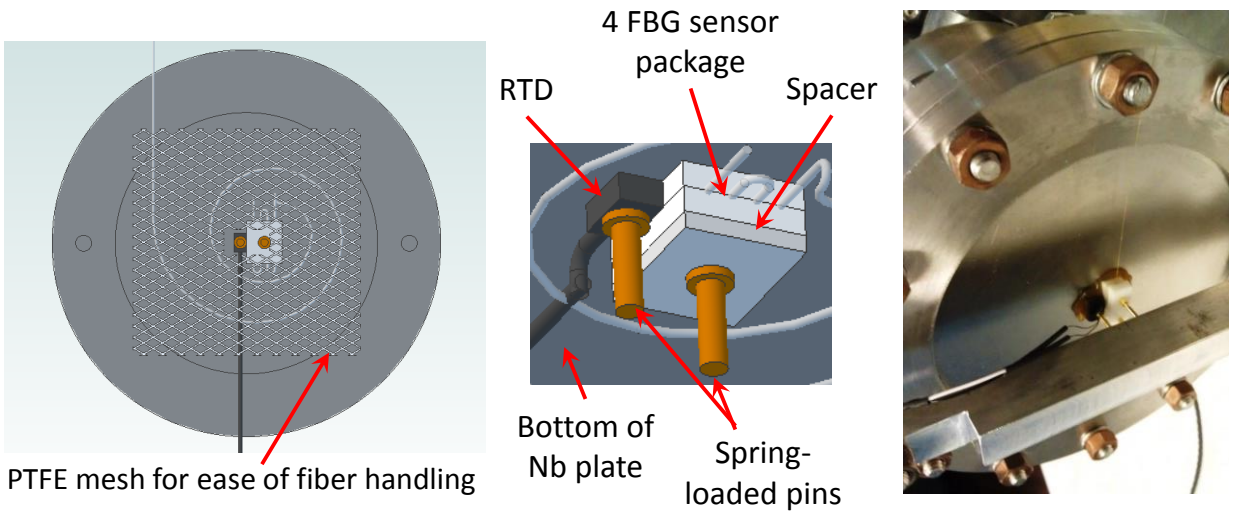

Figure 23. Schematics of JLab thermal distribution measurement setup. Left: schematics of the experiment (the heater pin is on the opposite side of the flange exactly over the boundary between RTD and fiber optic package); center: illustration of the sensor arrangement in the set-up, right: photo of the sensors mounted on the flange at JLab.

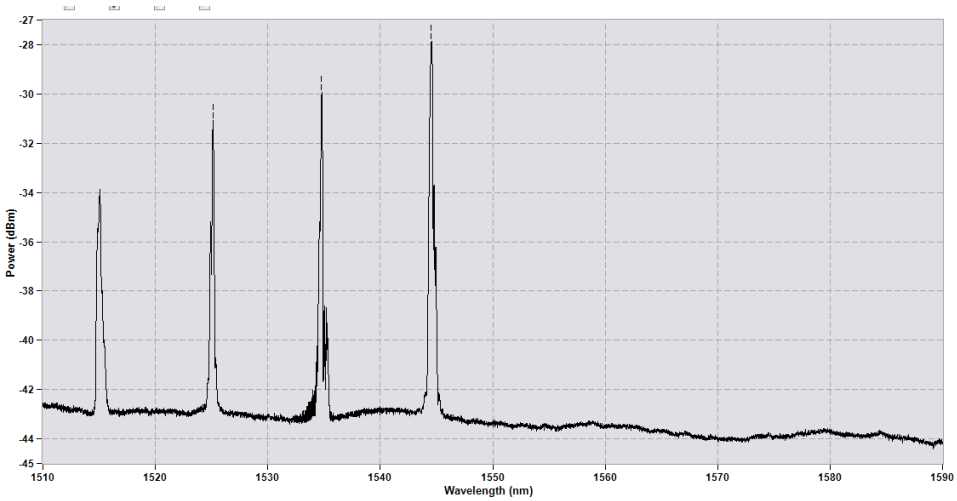

Figure 24. Reflectivity of 4-sensor array tested at JLab measured at 4.2K.

Few comments need to be made in regard to this setup to keep in mind while interpreting the collected experimental data:

1) The Si diode (Scientific Instruments) reference RTD that was used for testing the sensors during cool down and heat up from 4K to 300K was located which was at approximately the same height as the fiber sensor but at ~20 cm radial distance from the fiber optic sensors (10s of cm). This is one of the reasons during the dynamic cooling and heating the temperature difference between the readings of fiber optic and reference RTD sensors is expected to be quite substantial.

2) The thermal mass of RTD package and of fiber optic package are quite different, as it is apparent from Figure 23 the fiber optic sensor package is sizably more thermally massive than reference RTD co-located with the package so, again, perfect correlation between the data during the dynamic testing is not expected.

3) Due to different geometry of the reference RTD and fiber optic package the temperature distribution in both packages is expected to be quite different as well, so perfect correlation (or even correlation to 100mK) hardly can be expected as well.

4) Due to substantial length of the fiber between sensors (~60cm on average) and the constrained volume in the testing setup multiple turns of fiber with the small bend radius were required, with different number of turns for each sensor. This resulted in sizable optical losses for one sensor in an array (see Figure 24).

With these notes, we can review the testing results.

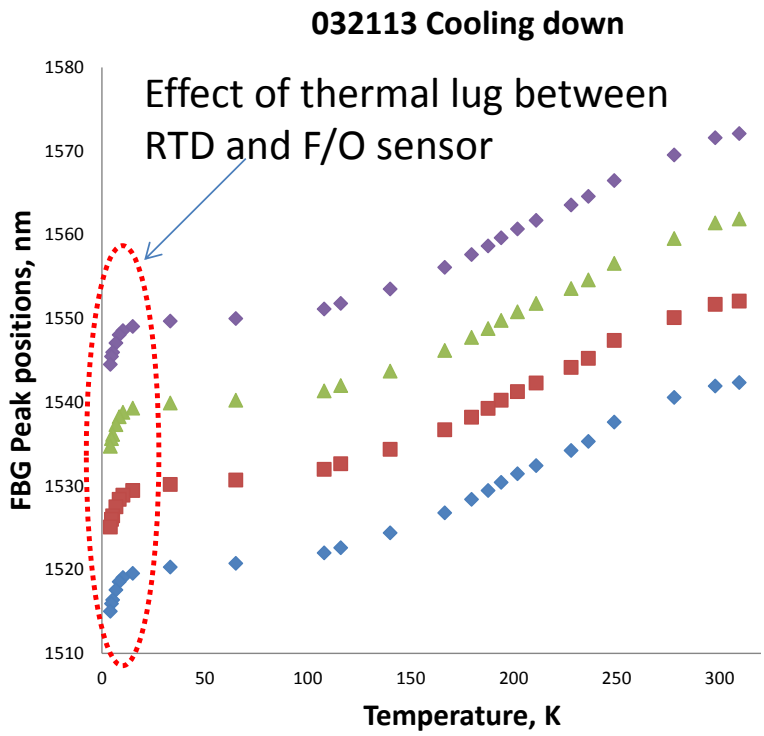

Figure 25. Response of four FBG sensors upon cooling from room temperature to 4.2K

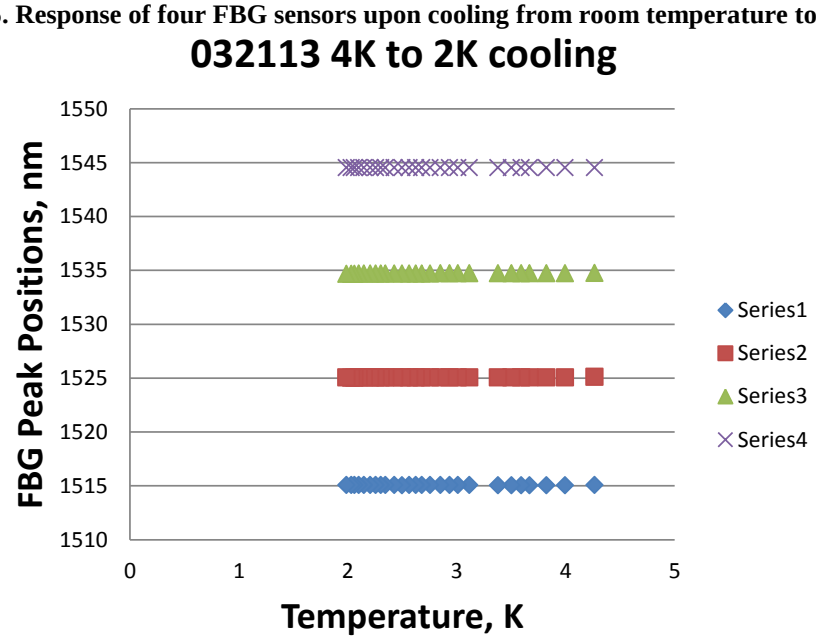

Figure 26. Response of the sensors during cooling between 4K and 2K.

The response of FBG sensors to the cooling down between the room temperature and 4.2K is shown in Figure 25. The temperature was measured by a Si diode (Scientific Instruments) which was at approximately the same height as the fiber sensor but at ~20 cm radial distance. The cooling rate was not constant over the temperature range: between the 4K and 6K the rate was ~2.5K/min, while between 6K and 16K it was ~5K/min, so the highlighted feature of apparent increase of sensitivity below 6K is at least partially due to a thermal lug effect.

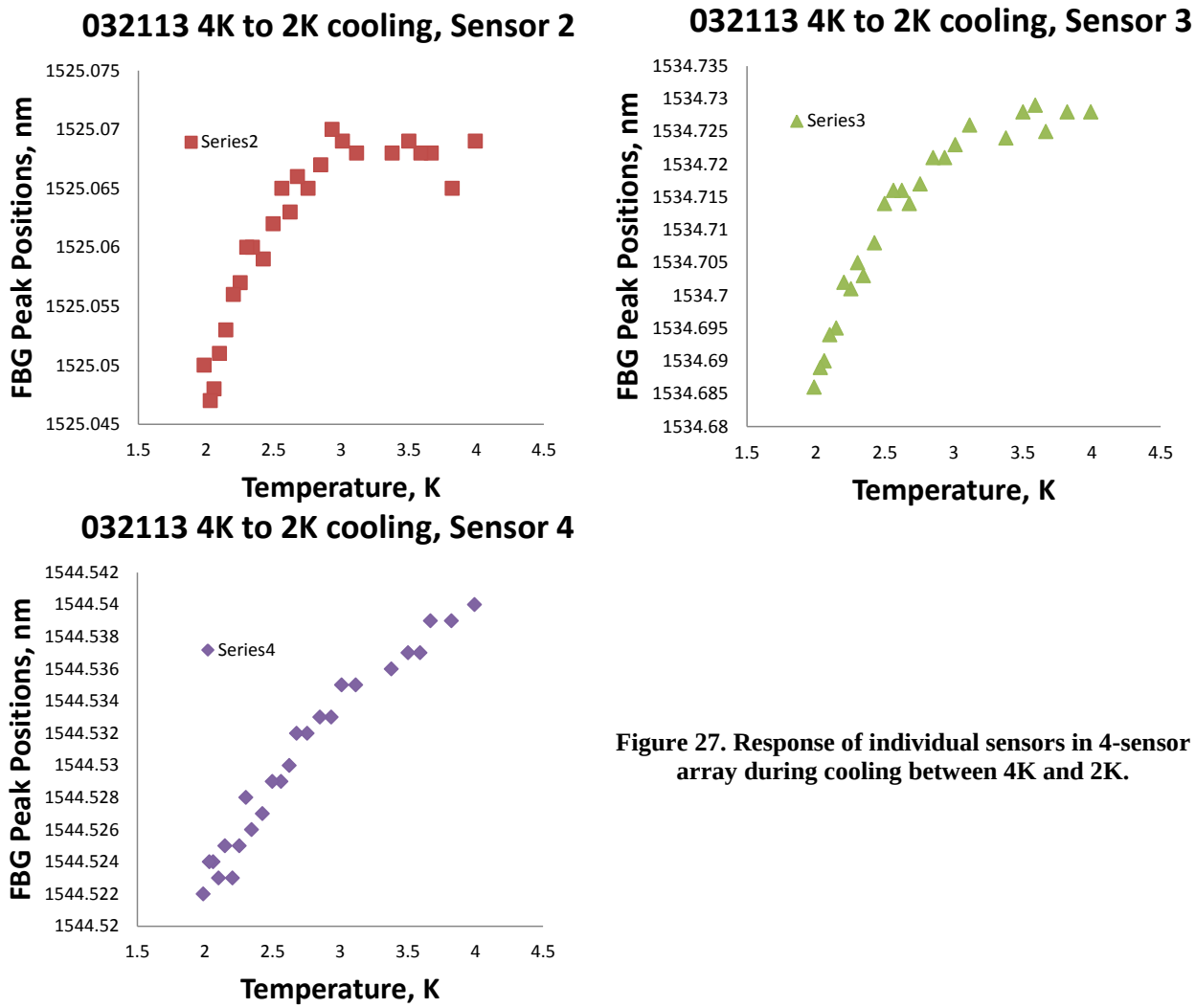

Figure 27. Response of individual sensors in 4-sensor array during cooling between 4K and 2K.

The cooling between 4K and 2K was done at much diminished cooling rate (~70mK/minute) by pumping on the He bath and the temperature was obtained from the He bath pressure. (the reference carbon-RTD co-located with fiber optic sensors was also calibrated during this cool-down). The behavior of fiber optic sensors during this cool down is illustrated in Figure 26 and Figure 27. It should be noted that the sensor with the lowest wavelength which experienced the largest losses due to fiber coiling exhibited sizable noise in the response –it's reflectivity spectrum not only sizably diminished but also deformed resulting in noise in identification of FBG peak position comparable to the effect of temperature change between 4K and 2K. The other 3 sensors exhibited very clear response at these wavelengths, as seen in Figure 27 with sensitivity varying between 9pm/K and 20pm/K, in line or slightly exceeding the expectations

based on testing of similar sensors at another setup (see discussion in previous section in relation to Figure 11 and Figure 12). The apparent increase of sensitivity between 2K and 3K observed on few sensors is not well understood at present. The explanation of the effect requires precise knowledge of the thermal expansion and mechanical moduli of the materials and components in the sensor package at these temperatures, which is missing at present. However, this experiment clearly show that the fiber optic sensors developed on this project demonstrate very significant sensitivity at 2K-4K range. These sensors not only show adequate sensitivity at an order of magnitude lower temperatures than other state of the art FBG sensors, but also exhibiting sensitivity comparable to the sensitivity of state of the art sensors at ~300K. With spectral resolution of the best interrogation instruments of 0.1pm, such sensors are expected to provide temperature resolution of between 5mK and 10mK. Moreover, if averaging will be implemented, it may even be better than that. It should be noted that two different 4-sensor packages were tested and similar results were reproduced on both of the packages. In another package, not discussed in this report two sensors showed higher than desired noise due to fiber coiling, so only two sensors were sufficiently sensitive at these temperatures.

It is also worth noting that no strain compensation was used on tested sensors. While strain-compensated packages were developed during the project, they were not tested at JLab due to constrains associated with the access to JLab equipment. Still, it is not expected that strain effects from Nb plate were significant since the sensors and the plate were separated with very low Youngs modulus thermal grease.

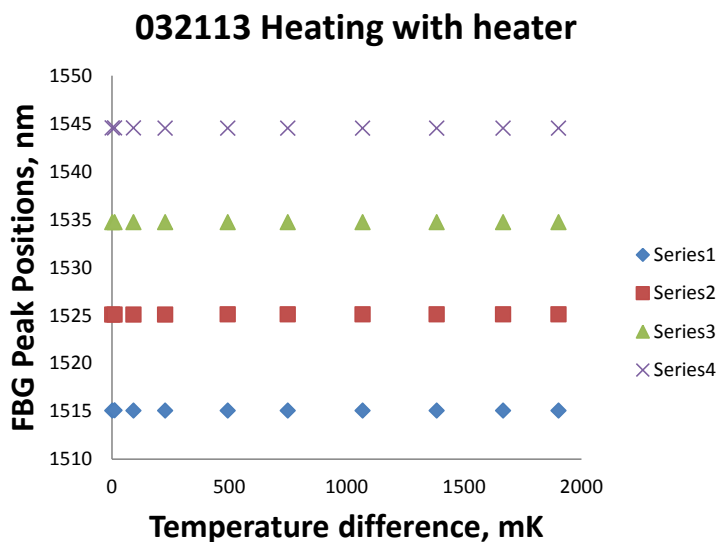

Figure 28. Response of the sensors during heating with the point heater while at 1.96K.

The last experiment that was performed involved detection of the thermal distribution in a Nb plate generated by point heater as discussed previously. The results of the testing are shown in Figure 28 and Figure 29. The 1st sensor showing temperature increase of ~2.5K, the 2nd sensor showed temperature increase of 0.7K, while the 3rd showed temperature decrease of ~1.4K based on calibrations as in Figure 27. While the slightly larger than measured by reference RTD temperature change response of 1st sensor can be explained by higher closer temperature in the sensing area of the sensor to that on the Nb plate surface due to less efficient heat removal by LHe (it probably indeed the case), and smaller temperature change measured by 2nd sensor (positioned ~twice further from the heating spot) is entirely expected, the negative temperature

change measured by the 3rd sensor is completely unphysical and probably represent an erroneous result. At present we don't have the explanation for such an effect. Still, such a demonstration, even imperfect, can be considered as a first ever convincing fiber optic distributed temperature monitoring below 12K.

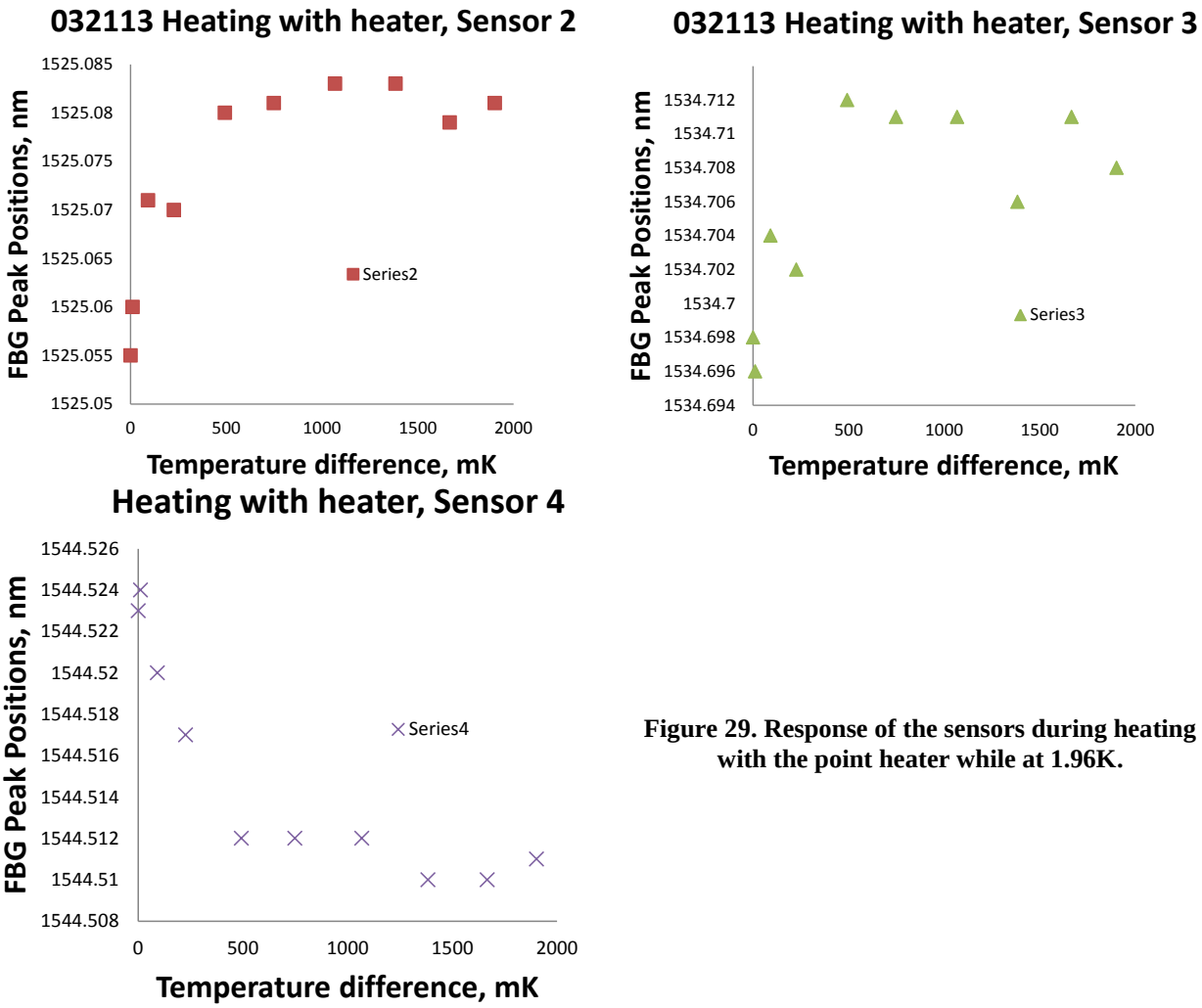

Figure 29. Response of the sensors during heating with the point heater while at 1.96K.

These experiments concluded testing and JLab. It should be noted that few sensors that were developed/fabricated were not tested due to time/funding limitations. The most interesting of those from our standpoint is strain-free, environmentally sealed package of the cryogenic temperature sensor as shown in Figure 30. If testing of such a sensor would provide positive results it would represent a product ready for immediate commercialization.

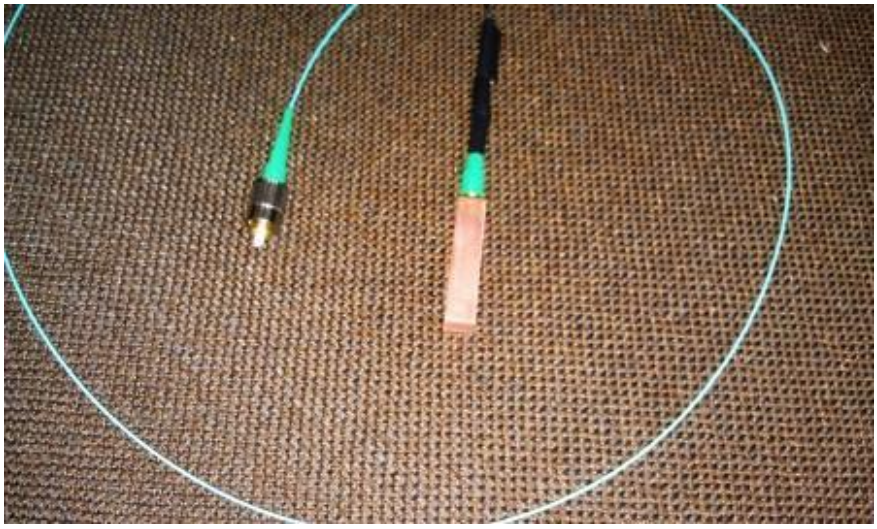

Figure 30. Photo of the packaged strain-free, environmentally sealed fiber optic cryogenic temperature sensor.

3.5 Conclusions and outlook

To summarize, the demonstrated temperature resolution of developed during the project sensor is by at least a factor of 60 better than that of the best multiplexible fiber optic temperature sensors reported to date. The demonstration was done with inexpensive fiber optic interrogator sm125 from Micron Optics which has 1pm wavelength resolution and no averaging implemented. Using ~60% more expensive (still quite affordable) sm130-500 model from Micron Optics with averaging 0.05pm wavelength resolution is achievable with 1Hz update rate.[47] With sensitivity of the sensors at 2-4K around 10pm/K, utilization of such an advanced interrogation unit is expected to result in resolution of ~2.5mK at these temperatures, by three orders of magnitude exceeding state of the art. It should be noted that up to 12 temperature sensors can be interrogated on the same fiber for full 2K to 400K temperature range measurements, or up to 80 sensors on the same fiber if only narrow (e.g., 2K to 77K) temperature range measurements are needed. With the cost of the instrument in the low $20k this not only will result in cutting the number of leads going to the feedthrough by a factor of 360, but also may provide a significant savings, since the instrument has 4 channels and can thus interrogate 80x4=320 sensors, resulting in ~$75/sensing point, sizably lower than for RTD readout. By using the expansion module (Channel Multiplexer, sm041), the total of 1280 sensors can be interrogated with the same interrogation instrument, bringing the cost per senor down to ~$35.

The first to date temperature distribution measurements with ~2.5mm spatial resolution was done with fiber optic sensors at 2K to4K temperatures. The repeatability and accuracy of the sensors were verified only at 183K, but at this temperature both parameters significantly exceeded (by at least a factor of 6) state of the art. Moreover, it was argued that the limiting

[47] http://www.micronoptics.com/uploads/library/documents/Datasheets/Micron%20Optics%20sm130.pdf

factor in identified repeatability and accuracy is the repeatability/accuracy of the calibration setup, not the sensor itself, so even more impressive numbers are expected.

While the developed sensor represents a very significant advancement to the state of the art, during the course of the project the team learned fabricating such sensors only one at a time, which makes the cost of each sensor significantly higher than what is desired for truly distributed sensing where 1000s to 10,000s sensors are to be used (although on par with the cost of similar room temperature fiber optic sensors from other commercial entities). In order to fabricate truly distributed and inexpensive in quantities sensors the technique of coating the fiber while fiber is drawn needs to be developed, which was outside of what could be accomplished on project budget. In this case the price per sensing and interrogation point is expected to drop to below $10.

4. Products developed under the award and technology transfer activities

4.1 Publications:

Oct. 2011: Results of joint work of MicroXact, Jlab and Virginia Tech were presented at 78th Annual Meeting of the Southeastern Section of the APS: E. See, V. Kochergin, L. Neely, M. Zaynetdinov, G. Ciovati and H. Robinson, "Negative coefficient of thermal expansion in (epoxy resin)/(zirconium tungstate) nanocomposites"

March 2012: Results of join work by MicroXact, JLab and Virginia Tech were presented at the APS Meeting, February 27-March 2, 2012, abstract #D24.001: E. See, V. Kochergin, L. Neely, M. Zaynetdinov, G. Ciovati, H. Robinson, "Zirconium tungstate/epoxy resin nanocomposites with negative coefficient of thermal expansion for all-dielectric cryogenic temperature sensors."

July 2012: Results of joint work by MicroXact and Virginia Tech were published: L. A. Neely, E. See, H. D. Robinson, V. Kochergin, "Thermal expansion of Cu(II)O nano- and micro-particles and composites at cryogenic temperatures," Phys. Stat. Sol. (b) (2012) doi: 10.1002/pssb.201248121

In publication at the time of report submission: L. A. Neely, V. Kochergin, E. See, H. D. Robinson, "Negative thermal expansion in zirconium tungstate/epoxy composites at low temperatures," submitted to Phys. Stat. Sol. (b)

Possibly more low-level conference presentations by Virginia Tech grad students that we are not aware of during report submission.

4.2 Web postings:

http://microxact.com/cryogenicthermometry.html

4.3 Networks or collaborations fostered:

Virginia Tech, Lake Shore Cryotronics, JLab

4.4 Technologies/Techniques:

Multiplexible cryogenic fiber optic sensors described in this report.

4.5 Inventions/Patent Applications:

Nov. 6, 2012: US Patent 8,303,176 "Cryongenic Fiber Optic Temperature Sensor and Method of Manufacturing the Same" by V. Kochergin.

4.6 Other products:

N/A